

Vibroacoustic methods for corrosion-state monitoring
in nuclear power plant secondary piping structures

By

Thomas Stilson

Thesis

Submitted to the Faculty of the
Graduate School of Vanderbilt University
in partial fulfillment of the requirements
for the degree of

MASTER OF SCIENCE

in

Mechanical Engineering

August 31, 2019

Nashville, Tennessee

Approved:

Douglas E. Adams, Ph.D.

Eric J. Barth, Ph.D.

Thomas J. Withrow, Ph.D.

To my friends and family

Acknowledgements

I want to express my deepest thanks to my advisor and committee chair, Professor Doug Adams, for his leadership during my time at Vanderbilt. Through his enthusiasm and patience, he showed me what a good scientist, engineer, and person can strive to be. I also want to thank my committee members – Professors Thomas Withrow and Eric Barth – for their insightful guidance along the way.

I was blessed to work at the Laboratory for Systems Integrity and Reliability (LASIR) among outstanding mentors and peers. I especially want to thank Dr. Sankaran Mahadevan, Dr. Pranav Karve, Dr. Cole Brubaker, Dave Koester, and Garrett Thorne for their valuable ideas and support on my research.

In addition, I was blessed with a 4-year undergraduate study in the Vanderbilt Mechanical Engineering Department, enrolled for the final 2 years in the Accelerated Graduate Program in Engineering. Madhavi and Jay Desai originally encouraged me to take on this challenge, and until I can pay their mentorship forward, I will remain in their debt for the doors they opened to me.

I want to thank the Vanderbilt Mechanical and Civil Engineering faculties for supporting both my undergraduate and graduate careers. I also want to thank Chris Lindsey, Amanda King, Liz Leis, and Aliceteen Morrow for their assistance with administrative challenges.

This work would not have been possible without the financial support of the Department of Energy Nuclear Energy Enabling Technologies (NEET) Program through grant DE-NE0008712. I especially appreciate the collaboration of Professor Kane Jennings and Liudmyla Prozorovska in the Vanderbilt Chemical and Biomolecular Engineering Department; whose remarkable work was an important catalyst for the research presented in this thesis.

Nobody has been more important to me in the pursuit of this project than the members of my family. I want to thank my parents; whose love and guidance are with me in whatever I pursue. I also want to thank my grandparents, who have kept me grounded in their wisdom, my brother, who has reminded me to stay humbly driven in all that I do, and the rest of my family members, who have each supported me immeasurably in their own ways towards the completion of this work.

Table of Contents

	Page
Acknowledgements.....	iii
Table of Tables	v
Table of Figures	vi
1. Background and State of the Art of Nuclear Power Plant Inspection.....	1
1.1 Corrosion in Nuclear Power Generation Facilities	2
1.2 Review of Risk-Based Inspection Practices	3
1.3 Augmentation to State of the Art: Embedded Vibroacoustic Sensor Networks.....	6
2. Background on Modal Analysis.....	8
2.1 Modal Expansion Theorem.....	8
2.2 Frequency Response Function Estimation.....	9
2.3 Experimental Modal Analysis and its Practical Limitations.....	11
3. Late-Stage Corrosion Detection Using Transmissibility Across Degrees of Freedom	13
3.1 Background Theory and Modelling	13
3.2 Overview of Testing Rig.....	18
3.3 Elbow Mode Shape Visualization with Experimental Modal Analysis.....	19
3.4 Mass Change Detection Using Transmissibility Function Estimation	24
3.5 Variability Between Elbow Removals and Reinstallations	37
3.6 Day-to-Day and Run-to-Run Variability in Transmissibility Function Estimation.....	39
3.7 Repetition of Mass Reduction Experiment	41
3.8 Effects of Operating Temperature and Pressure on Damage Index Calculation	44
3.9 Conclusions and Next Steps	51
4. Early-Stage Corrosion Detection with Smart Film Technology.....	52
4.1 Background on Smart Film Technology.....	52
4.2 Effects of Chelation on Vibroacoustic Behavior of Silicon Wafers	53
4.3 Implications of Smart Film Technology on the Nuclear Industry	69
5. Summary and Conclusions	71
References.....	73

Table of Tables

Table	Page
1-1: Common methods for nondestructive evaluation of pipe health	5
3-1: Additional mode shapes identified with torsional-bending characteristics	23
3-2: Mass removal stages on pipe elbow	28
3-3: Damage indices calculated at accelerometer 4 for each mass removal trial, 10-12 kHz	35
3-4: Damage indices calculated at accelerometer 5 for each mass removal trial, 10-12 kHz	36
4-1: Model parameters of the bare silicon wafer and test setup used	63
4-2: Tabulated natural frequencies from analytical model (Hz)	64
4-3: Tabulated natural frequencies from numerical model (Hz).....	64
4-4: Error between analytical and numerical models of silicon wafer.....	64
4-5: Comparison of selected analytical and numerical mode shapes for bare silicon wafer.....	65

Table of Figures

Figure	Page
3-1: Idealized model of pipe cross-section without damage.....	13
3-2: Pipe cross-section with non-axisymmetric damage.....	16
3-3: Diagram of pipe section with labeled flexing-body motions.....	17
3-4: Overview image of testing rig.	18
3-5: Pipe elbow shown with accelerometers mounted.....	19
3-6: Sample average input power spectrum from modal hammer used on test bed.....	20
3-7: Mode shape visualization of elbow at 9900 Hz with home view shows torsion motion between accelerometers 4 and 5	21
3-8: Mode shape visualization of elbow at 9900 Hz with top view shows torsional motion near accelerometer 2, indicating potential for observation of bending-torsion modal coupling.....	22
3-9: Pipe elbow with 6 triaxial accelerometers	24
3-10: Diagram of accelerometer on elbow with given angle offset from global x -direction.....	25
3-11: Relative transmissibility contour of baseline pipe elbow	27
3-12: Top view of elbow with area of mass removal shown in yellow	28
3-13: View of inner diameter of pipe elbow with material ground away	29
3-14: Pipe elbow before (left) during (middle) and after (right) material removal.....	29
3-15: Milwaukee 2” die grinder and carbide bit used to remove material	29
3-16: Relative transmissibility contour with 0.3% mass removed from elbow	30
3-17: Relative transmissibility contour with 0.5% mass removed from elbow	30
3-18: Relative transmissibility contour with 0.75% mass removed from elbow	31
3-19: Relative transmissibility contour with 1% mass removed from elbow	31
3-20: Relative transmissibility contour of elbow with 1.25% mass removed.....	32
3-21: Relative transmissibility contour of elbow with 1.5% mass removed.....	32
3-22: Relative transmissibility plots between accelerometers 4 and 5, 9500-12500 Hz.....	33
3-23: Boxplot of damage index vs percent mass removed on elbow at accelerometer 4.....	35
3-24: Damage index vs percent mass removed at accelerometer 5.....	36
3-25: Accelerometer 4 damage index boxplots for elbow removal variability trial, 1.5% mass reduction	38
3-26: Accelerometer 5 damage index boxplots for elbow removal variability trial, 1.5% mass reduction	38
3-27: Damage index calculated at accelerometer 4 over 1 week of operation, 10-11 kHz.....	40
3-28: Baseline damage index calculated at accelerometer 5 over 8 days of operation, 10-12 kHz	41
3-29: Degraded gasket after use in first mass removal experiments.....	42
3-30: Configuration of second elbow used in mass removal experiment	43
3-31: Damage index vs mass reduction for second pipe elbow, accelerometer 4.....	43
3-32: Damage index vs mass reduction for second pipe elbow, accelerometer 5.....	44

3-33: Temperature vs damage index for damaged pipe elbow mounted with EPDM rubber gaskets. Trial 1 of 2 indicates strong positive correlation between temperature and damage index	45
3-34: Temperature vs damage index for damaged pipe elbow mounted with EPDM rubber gaskets. Trial 2 of 2 indicates correlation is repeatable between days of operation.....	46
3-35: Pressure vs damage index for damaged pipe elbow with comparison to healthy baseline pipe elbow at 5 psi and 80°C	47
3-36: Damage index vs pressure on elbow mounted with EPDM rubber gasket shows positive correlation between pressure and damage index.....	48
3-37: Temperature vs damage index for the second elbow with 1.50% mass removed, using Aramid/Buna n gasket material.....	49
3-38: Pressure vs damage index plot for second elbow with 1.50% mass removed using Aramid/Buna-N gasket material, indicating similar trend between pressure and damage index.	50
4-1: Silicon wafer before (left) and after (right) chelation. Visually, only a slight yellow coloration in the chelated film distinguishes their appearance	52
4-2: Side-view diagram of test fixture for Si wafer trials	54
4-3: Test fixture (left) with Si wafer installed (right)	55
4-4: Frequency vs frequency response function for bare wafer, with first three peaks labeled	56
4-5: Frequency vs frequency response function for wafer 1, with 2200 Hz and 6100 Hz peak highlighted for further investigation.	57
4-6: Frequency response function for wafer 1 between 5600 Hz and 6600 Hz, illustrating a trend between stage of film and peak amplitude.....	58
4-7: Damage indices for each stage of chelation in wafer 1, from 5.6-6.6 kHz, show a positive relationship between chelation and damage index.	59
4-8: Frequency response function peak at 6100 Hz for wafer 2	60
4-9: Damage indices for each stage of chelation on the second wafer.	61
4-10: First frequency response function peak for wafer 1 (left) and wafer 2 (right) show peak frequency increase with chelation of the film.	62
4-11: Boxplots of damage indices calculated from 1 kHz to 3.5 kHz for wafers 1 and 2 indicate opposite trends in damage index for each wafer. Note that axes are not scaled equally.	62
4-12: 3-dimensional rendering of wafer modeled with added mass of accelerometer; mesh shown.....	67
4-13: First four numerically modeled mode shapes of silicon wafer with added accelerometer mass	67

1. Background and State of the Art of Nuclear Power Plant Inspection

The work presented herein supports a widespread paradigm-shift in inspection and maintenance practice to a specific industrial application. Real-time degradation state monitoring through the use of advanced instrumentation, data analytics, and software automation has the potential to significantly reduce both operating costs and incidence of missed diagnoses across sectors [1].

Chapter 1 consists of a brief introduction to the state of the nuclear power industry, and it provides context for the research results described in later chapters. Key topics covered include the concept of Risk-Based Inspection and its limitations, the history of risk-based inspection and its application in the nuclear power industry, and success rates of modern risk-based inspection practices in nuclear power facilities,

Chapter 2 contains a brief review of modal analysis. The key concept in this chapter is that vibrational modes in a structural component such as a pipe follow the principle of superposition. Because of the superposition principle, modes most sensitive to a selected type of damage can be chosen individually and meaningfully studied for insights into the overall state of damage of the system.

In Chapter 3, operating transmissibility function estimation will be used as a method for damage detection in late-stage corrosion situations. In this paper, ‘late-stage’ corrosion refers to corrosion which has advanced to the point where traditionally measurable mass and geometry changes have occurred on the pipe section of interest. In Chapter 4, frequency response function estimation will be used to characterize the mechanical properties of smart film samples before and after ion-capture. The application of this technology will be analyzed in the context of early-stage corrosion detection. In this context, ‘early’ stage corrosion refers to corrosion that occurs before a measurable change in mass or geometry occurs, such that iron ions are released into the working fluid but the actual change in mass and geometry of the pipe section is not detectable by traditional methods. The necessary background for understanding the relationship between vibration and degradation is given in Chapter 2. Chapter 5 contains final conclusions and summarizes areas of future work.

1.1 Corrosion in Nuclear Power Generation Facilities

The most recently released Reference Data Series published by the International Atomic Energy Agency reported that at the start of 2018, there were 448 nuclear reactors online globally with a combined capacity of 391.7 GW(e), generating 2500 TW(e)h in 2017 [2]. This report indicated that an additional 59 units were under construction globally. The 2018 World Nuclear Performance Report stated that the global average capacity factor, or ratio of achieved production to maximum theoretical production with 24/7 operation, of these plants was 81% [3]. As of June 2019, the United States had 97 operational reactors in its fleet [4], with an average age of 39 years [5].

Pipe corrosion management is a critical issue in nuclear power plant operations [6],[7]; these facilities employ miles of piping to carry working fluids that drive generators and exchange heat. Because cooling loops in nuclear power plants operate at high temperatures and pressures, pipe wall corrosion is a necessary consideration. In spite of this, the Component Operational Experience, Degradation and Ageing Programme Group reported that 4.6% of recorded pressure boundary failure events were caused by less-than-adequate reliability and integrity management [7], implying that the vast majority of pipe failures in nuclear power plants occur in spite of adequate reliability and integrity management practices.

According to a report published by the Electric Power Research Institute in 1996, there were a reported 1511 piping failures incidents in US nuclear power plants between 1961 and 1995 [8]. This report stated that erosion-corrosion, or the chemo-mechanical degradation that occurs when turbulent flow impinges on metal surfaces [9], accounted for 43% of all failures during this time period. It was also indicated in this report that although improved risk management strategies and new reporting requirements significantly reduced the frequency of reported failures after 1983, erosion corrosion was the only failure mode that prevented failure rates from continuing to decrease.

A more comprehensive global data exchange program was created by the Organization for Economic Co-operation and Development and the Nuclear Energy Agency in 2002 to collect and monitor piping failure events from nuclear power plants around the globe. In the final document for this partnership submitted in 2012, it was reported that after approximately 9,300 reactor-years

of operation, 3746 nuclear power plant pipe failure events were recorded from 321 operating plants. Of these failure events, 57% were caused by some variant of corrosion (corrosion, erosion-corrosion, flow-accelerated corrosion, corrosion-cracking) [10].

The motivation behind this research is drawn from insights gained from the historical data on pipe failures in nuclear power plants. These data suggest that pipe-wall corrosion plays a significant role in reducing the reliability, operability, and cost-effectiveness of nuclear power plants [6], both in terms of public safety and economic outcomes of power plant operators.

Although the daily cost of unplanned outages is largely determined by the value of lost generating revenue and the replacement power cost at the time of the outage [11], the total cost of downtime has been reported to exceed \$1 million per day at specific plants [11], [12]. The lost margin costs alone have been generally estimated to exceed \$500,000 per day for off-line plants, putting the overall bill at approximately \$1.3 million per day across the industry [13]. For plants struggling to compete with traditional energy sources [14], each day of unplanned lost production constitutes a significant barrier to remaining cost-effective. The thesis of this research is that state monitoring techniques can be improved to address pipe wall corrosion and ultimately, after sufficient testing and evaluation in power plants, such monitoring can make plants safer to operate for longer periods of time between major inspections while simultaneously reducing the sunk cost of outages and improving inspection efficiency.

1.2 Review of Risk-Based Inspection Practices

Risk-based inspection is based on estimating the potential consequence and likelihood of different failure mechanisms in an operating facility. Cost and probability of a given failure are used to calculate risk. The risk associated with that failure mode determines the regularity with which the associated part or subsystem is inspected and maintained [15].

Because risk-based inspection is based on anticipation of failure, a strong understanding of the processes at play in a power plant is necessary to account for possible failures. In the aftermath of major failure events, industry-wide inspection standards are reviewed and changed to account for the new understanding of previously unconsidered dangers in operation [16], [17], [18].

Unfortunately, equipment failure in the nuclear industry can pose extreme costs to operator financial bottom lines, human health outcomes in affected regions, and public opinion of nuclear power generation [11], [12], [19].

Historically, nuclear plants were designed with high standards of safety, so inspection and maintenance were not anticipated as necessary parts of plant maintenance [20]. As operator experience revealed that degradation and component failure were unavoidable, deterministic risk management strategies were developed in the American Society of Mechanical Engineers (ASME) Boiler and Pressure Vessel Code, Section IX [21], with later revisions expanding the scope and application of this guidance.

However, operator experience also showed that the ASME guidance was insufficient in evaluating the risk of specific components. Because the Boiler and Pressure Vessel Code did not account for specific plausible degradation mechanisms in assessing a component's risk, the most likely failure modes for critical components were often overlooked [20]. It has also been posited that roughly 80% of the risk in a facility comes from approximately 20% of the equipment [22], but the ASME code alone only called for general sampling of components to account for a generalized form of degradation. In light of this fact, it was determined that a focus on the small subset of equipment at high-risk would also lead to improved risk-management outcomes.

Therefore, the modern approach to inspection uses probabilistic models to better calibrate risk levels for components. By integrating previously observed degradation mechanisms with the ASME baseline of materials, pressure levels, and operating stress levels, a more accurate probability of failure can be obtained, thus improving the accuracy of risk assessments and ensuring that inspection resources are appropriately allocated [20]. Risk-informed in-service inspection has evolved to become the industry standard in nuclear pipe inspection practice. As probabilistic risk assessment models became mainstream in the industry, the average industry capacity factor increased while the core damage frequency, or likelihood of a severe fuel-damaging accident, has steadily decreased [23]. The adoption of risk-informed in-service inspection based on probabilistic risk assessment corresponded to a **fourfold** reduction in core damage frequency across the industry.

The in-service inspection approach used in nuclear power plant facilities is largely based on volumetric and surface nondestructive evaluation methods [24], [25]. A thorough review of nondestructive evaluation techniques used in metallic pressure boundaries is given in [24].

Table 1-1 summarizes the set of methods most commonly used in nuclear power plants for both pipe thickness measurements and corrosion monitoring. A key commonality to the risk-informed in-service inspection methods listed below is that they require on-site operators and are fundamentally point-wise in their application. For a power plant, inspection either becomes extremely local to the highest-risk sections or time-consuming and costly, both in terms of technician labor-hours and generation hours lost. Furthermore, the majority of inspections find parts which meet acceptable operating criteria. For example, from 1997 to 2017, Over 600 weld examinations were performed at the Indian Point nuclear reactor units, with over 90% of these examinations meeting acceptable criteria [7]. Moreover, insulation must be removed to access pipe walls directly to apply most of the methods in Table 1-1; therefore, they are costly to apply and require downtime in a facility, significantly limiting the frequency with which they can be used.

Table 1-1: Common methods for nondestructive evaluation of pipe health

Method	Advantages	Disadvantages
Liquid Penetrant Testing	Sensitive to surface flaws, large areas covered, visual	Limited to surface flaws, direct access to pipe surface needed
Magnetic Particle	Low-cost, fast inspection, portable	Maximum sensitive depth ~15mm
Ultrasonic	Thickness measurement and high sensitivity to flaws	Surface accessibility required; manual operation requires training
Eddy current	Non-contact, highly precise, high-temperature	Cannot detect flaws deep in a part
Acoustic emission testing	Does not require input energy source, detects emission from crack formation	Requires significant technical knowledge to use, sensitive to background noise
Thermography	Quick, provides visual inspection information of a part based on heat transfer properties	Becomes less effective as material thickness increases
Electrochemical Potential	Basic indicator of corrosion potential	Not a direct measurement; no information on rate of corrosion
Radiography	Good for detecting corrosion under insulation due to water trapping, able to calculate remaining pipe wall thickness	Relatively small measurement area

Additionally, the corrosion detection methods listed above do not provide directly measurable rate-of-corrosion data. They provide information about where corrosion could be occurring, but real-time information about the rate of corrosion is not obtained.

1.3 Augmentation to State of the Art: Embedded Vibroacoustic Sensor Networks

The challenge associated with risk-informed in-service inspection is that inspection resources are finite. Intuitively, to prevent pipe failure, either increased spatial or temporal resolution of inspection is needed in high-risk pipe sections to detect degradation, prevent failure, and reduce risk. Embedded vibroacoustic sensor networks are an attractive concept for augmenting the inspection capabilities of facility personnel because these networks address both temporal and spatial resolution needed to reduce risk.

With dedicated vibroacoustic sensors installed on pipe walls during plant operation, real-time operating data can be used to detect local changes in dynamic properties of an instrumented section of pipe. Estimated transmissibility functions have been shown to be highly sensitive to local changes in mass and stiffness [26], [27]. It has been shown that pipe fittings like elbows and joints are at especially high risk of degradation because flow around these joints can cause non-axisymmetric degradation of pipe wall material [28], [29]. Therefore, on these high-risk sections, tuned sensor networks can be used to track differential indicators of damage in conjunction with regular inspection cycles.

Additionally, recently developed smart film technology [30] has the potential to amplify early mass-transfer effects on vibroacoustic response.

The smart films have been demonstrated to capture iron ions out of low-concentration solution and use the iron to modulate the complex shear modulus of the films. Because of this, these films may be able to translate the early onset of corrosion on the inside of a pipe section into locally detectable changes in vibroacoustic properties measured on the outside of a pipe.

The proposed sensing technology should not be seen as a replacement for trained inspectors, but as an additional source of information for plant operators to manage risk. The following work is an exploration of late-stage corrosion-state monitoring with the use of

transmissibility function estimation, as well as a discussion of early testing on smart film vibroacoustic property modulation. Information from these sources would improve temporal resolution of inspection information by automating the data acquisition and recording process with operating flow-induced vibrations as the primary forcing input to the system. The contributions in this thesis establish one such analytical approach with operating data and characterize sources of variability in damage-state monitoring calculations based on this approach.

2. Background on Modal Analysis

In Chapter 2, a brief review of the math used in later analyses is described. The fundamental principles of modal analysis are reviewed, and frequency response function estimation is discussed. The principle behind transmissibility function estimation is treated here as well, with further elaboration in Chapter 3, Section 1.

2.1 Modal Expansion Theorem

The modal expansion theorem is the foundation for modal analysis [31]. This theorem states that any response of any system with multiple degrees of freedom can be expressed as a linear, weighted sum of its responses at the system natural frequencies. For a system with n degrees of freedom, any kinematically allowable response can be described with a sum of its n modes.

For a lumped parameter system with n degrees of freedom, this theorem can be expressed as:

$$\{x(t)\} = \sum_{i=1}^n \{u\}^i q_i(t) \quad 2-1$$

Here, $\{x(t)\}$ represents the response vector in general coordinates, $\{u\}^{(i)}$ represents the i^{th} mode shape, and $q_i(t)$ corresponds to the i^{th} time-dependent behavior in natural (modal) coordinates. The power of this theorem is that the motion of a complicated n -degree of freedom system can be decomposed into its orthogonal modal components and solved as a series of n independent, 2^{nd} order systems. The solutions to these equations can then be re-assembled from modal to general coordinates to retrieve the actual response of the system.

For distributed systems with infinite degrees of freedom, where damping can be assumed to be relatively small, the principle of orthogonal modes allows for the selection of only the modes that ‘significantly’ contribute to a given system’s dynamic behavior. Because of this, the modal expansion theorem can be applied to selected modes of interest in a given application and produce usable results.

2.2 Frequency Response Function Estimation

Building on the concept of modal expansion, frequency response function estimation is the practice of estimating the frequency-domain transfer function of a system over the sum of all practically observable modes. Performed with a measured reference input and measured output, this estimation involves decomposing input and response time-histories into the frequency domain, calculating their power spectra, and using these spectra to estimate the frequency response function [32].

Note that frequency response function is a system property. This property can change over time due to damage, change in material properties (thermal variations, fatigue, etc.) or any other change in dynamic properties affecting a given mode of vibration.

The frequency response function is estimated with 5 main steps. Craig and Kurdila [32] give an in-depth discussion of this topic, which is summarized here as both theoretical background and explanation of later data analysis techniques used in this research. For an input signal $x(t)$ and a response signal $y(t)$, the one-sided Fourier Transform is estimated. For this work, a one-sided Fast Fourier Transform (FFT) algorithm is used to estimate the Fourier Transform of each signal.

$$\begin{aligned} X(\omega) &= fft(x(t)) \\ Y(\omega) &= fft(y(t)) \end{aligned} \tag{2-2}$$

The auto-power spectra are calculated by element-wise multiplication, where a^* denotes the complex conjugate of a .

$$\begin{aligned} G_{xx}(\omega) &= X(\omega)X^*(\omega) \\ G_{yy}(\omega) &= Y(\omega)Y^*(\omega) \end{aligned} \tag{2-3}$$

Similarly, the cross-power spectra between input and response are calculated by element-wise multiplication.

$$\begin{aligned} G_{xy}(\omega) &= X(\omega)Y^*(\omega) \\ G_{yx}(\omega) &= Y(\omega)X^*(\omega) \end{aligned} \tag{2-4}$$

Typically, multiple input-response measurements are made for frequency response function estimation so that an average can be made to reduce random error. At this stage, average spectra are calculated from the sampled power spectra vectors.

$$\tilde{G}_{xx}(\omega) = \frac{1}{N_{avg}} * \sum_{n=1}^{N_{avg}} G_{xx,n}(\omega) \quad (2-5)$$

A similar equation is used to calculate the other average spectra. With the average spectra, the frequency response function can be estimated. Craig and Kurdila give three methods for estimating frequency response function:

$$H_1(\omega) = \frac{\tilde{G}_{yx}(\omega)}{\tilde{G}_{xx}(\omega)}$$

$$H_2(\omega) = \frac{\tilde{G}_{yy}(\omega)}{\tilde{G}_{xy}(\omega)} \quad (2-6)$$

$$H_v(\omega) = \sqrt{H_1(\omega)H_2(\omega)}$$

In this work, an H_1 estimator is used. This is because the H_1 estimator is sensitive only to input noise. In the experiments involving frequency response function estimation, it was seen that the input noise level was lower than the output noise.

Finally, a measure of linear dependence of the output on the input is given by the coherence:

$$\gamma^2 = \frac{H_1(\omega)}{H_2(\omega)} \quad (2-7)$$

Coherence is a useful tool in evaluating the quality of data during collection and for verifying that a given modal response is truly caused by the measured input. The closer the coherence value of a frequency response function is to unity, generally speaking, the more confident an experimentalist can be that the measured response linearly correlated with the measured input.

2.3 Experimental Modal Analysis and its Practical Limitations

Experimental modal analysis with the use of forced vibration testing is a well-developed field with widespread application in the automotive and aerospace industries [33]. In experimental modal analysis, a forcing input into a system is measured simultaneously with the response, and from the analysis of the forced input and response, accurate estimation of frequency response function and modal parameters can be obtained. Experimental modal analysis has evolved to become the accepted method of collecting and analyzing vibration data on test specimens where it is feasible to do so.

In smaller structures, such as automotive and aerospace components, a hammer with a force transducer (i.e. a modal hammer) may be used to provide an impulsive-type input with relatively even frequency content across a range of interest. The challenge in conducting experimental modal analysis on infrastructure-scale systems is ensuring that the input power is large enough in amplitude and wide enough in frequency content to generate measurable response relative to background noise inherent in the system (wind, car/foot traffic, seismic tremors) [34].

To conduct experimental modal analysis on large civil engineering structures requires cumbersome actuators, long setup times, and partial-to-complete service closures in some cases. Drop weights, shaker actuators, and eccentric mass vibrators are used to generate forcing input for such analysis of large structures. Due to the high cost of transportation, setup, and safety measures, forced vibration testing is not commonly used in infrastructure-scale applications [35].

In the case of nuclear power plant piping systems, employing large actuators for modal testing would impose significant additional cost on operators without guaranteeing improved corrosion detection abilities. Additionally, experimental modal analysis has been shown to offer diminished returns in modal parameter estimation when compared to an output-only approach [36]. Broadly referred to as operational modal analysis, output-only techniques use only a system's measured response to ambient/operating conditions to evaluate modal parameters.

The basic mathematical tools used in operational modal analysis are identical to those used in experimental modal analysis. The difference is that instead of calculating system frequency response function with a known forcing input, a reference 'input' sensor is chosen from a sensor array to determine the relative response with respect to that reference.

The ratio of auto power spectra between two response time histories can also be calculated to give an estimation of the transmissibility function, or magnitude of frequency response function, between those two responses.

$$T_{x \rightarrow y}(\omega) = \frac{G_{yy}(\omega)}{G_{xx}(\omega)} \quad (2-8)$$

In Chapter 3, transmissibility functions are estimated in this way, using operating data to calculate auto power spectra instead of a forced input. Note that any reference measurement can be taken as the ‘input’ to calculate operational modal analysis frequency response functions, but for this work a focus on transmissibility function estimation is maintained. The ratio between the operating transmissibility functions of a healthy pipe elbow and a damaged pipe elbow will be shown to vary with the degree of damage in Chapter 3.

3. Late-Stage Corrosion Detection Using Transmissibility Across Degrees of Freedom

The goal of this chapter is to develop a tractable model of a pipe cross-section and use this model to detect mass anomalies in an operating pipe elbow. A two degree of freedom pipe cross-section is analyzed with a localized mass change to simulate corrosion. This model is applied to selected bending and torsional modes of a pipe elbow, which were measured and animated using experimental modal analysis. Relative transmissibility calculations were used to calculate a damage index which was shown to vary with the degree of mass removal in a pipe elbow.

3.1 Background Theory and Modelling

Consider a two degree of freedom model of a pipe cross section, shown in Figure 3-1. In this example, damping is assumed negligible for simplicity.

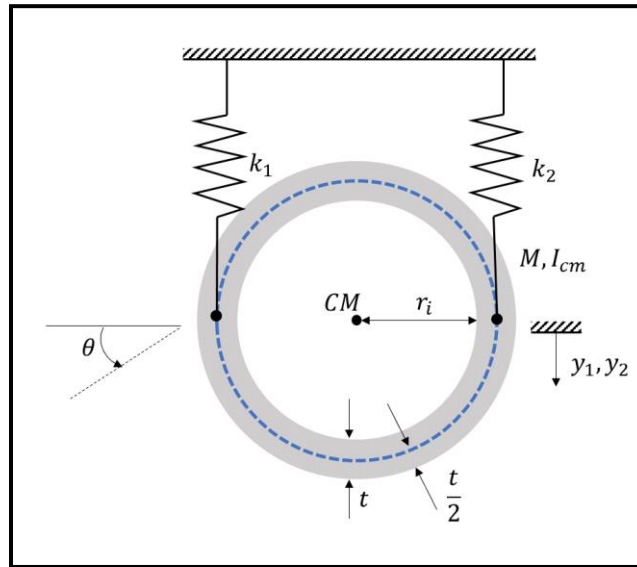


Figure 3-1: Idealized model of pipe cross-section without damage

The free-response equations of motion can be obtained using Newton's Laws of Motion, where $r_0 = r_i + \frac{t}{2}$, the displacement y_{cm} is of the center of mass, and it is assumed that $k_1 = k_2$

(the distinction between springs is made to distinguish two points of support). It is also assumed that $y_{cm} \approx y_2 + r_0\theta$ for small angular displacements.

Solving the free response of the system given in Figure 3-1 leads to the equations of motion:

$$\begin{bmatrix} m & 0 \\ 0 & I_{cm} \end{bmatrix} \begin{Bmatrix} \ddot{y}_{cm} \\ \ddot{\theta} \end{Bmatrix} + \begin{bmatrix} 2k_1 & 0 \\ 0 & 2k_1 r_0^2 \end{bmatrix} \begin{Bmatrix} y_{cm} \\ \theta \end{Bmatrix} = 0 \quad (3-1)$$

Using these equations of motion to solve the generalized forced response of the system leads to:

$$\underline{M}\ddot{x} + \underline{k}x = Fe^{j\omega t} \quad (3-2)$$

Here, the underbar indicates mass and stiffness matrices of the system, and it is understood that x and F are n by 1 vectors corresponding to the number of degrees of freedom of the system. Assuming linear behavior, this arrangement returns solutions of the form:

$$\begin{aligned} x &= xe^{j\omega t} \\ \dot{x} &= (-\omega^2)x e^{j\omega t} \end{aligned} \quad (3-3)$$

Which gives rise to the impedance matrix:

$$[-\omega^2 \underline{M} + \underline{k}]x = F \quad (3-4)$$

Where

$$\begin{aligned} Z &= -\omega^2 \underline{M} + \underline{k} \\ \Rightarrow Zx &= F \\ \Rightarrow x &= Z^{-1}F \end{aligned} \quad (3-5)$$

The transfer function matrix H is defined as the inverse of the impedance matrix Z , which for a two degree of freedom matrix with diagonal symmetry is given by

$$H = Z^{-1} = \frac{\begin{bmatrix} Z_{22} & -Z_{21} \\ -Z_{21} & Z_{11} \end{bmatrix}}{\|Z\|} = \begin{bmatrix} H_{11} & H_{12} \\ H_{12} & H_{22} \end{bmatrix} \quad (3-6)$$

Note that qualitatively, a given transfer function H_{ij} can be interpreted as the response along the i^{th} degree of freedom due to a unit forcing input along the j^{th} degree of freedom. Using given system parameters, the motion of the pipe cross-section can be expressed as:

$$x(\omega) = HF(\omega) = \frac{1}{\|Z\|} \begin{bmatrix} 2k_1 r_0^2 - \omega^2 I_{cm} & 0 \\ 0 & 2k_1 - \omega^2 m \end{bmatrix} F(\omega) \quad (3-7)$$

where the characteristic denominator is

$$\|Z\| = (k_1 + k_2 - \omega^2 m)(k_2 a^2 - \omega^2 I_{cm}) - (k_2 a)^2 \quad (3-8)$$

Transmissibility can be defined as the ratio between two elements of the forced response matrix. This physically corresponds to the magnitude of the frequency-domain transfer function between these two response components (i.e. how they interact with each other).

$$T_{ij \rightarrow kp} = \frac{H_{kp}}{H_{ij}} \quad (3-9)$$

Observing the system response between degrees of freedom for a unit input in the y_{cm} degree of freedom shows that:

$$\left. \frac{\Theta(\omega)}{Y_{cm}(\omega)} \right|_{y_{cm}} = \frac{0}{2k_1 r_0^2 - \omega^2 I_{cm}} \quad (3-10)$$

Similarly,

$$\left. \frac{Y_{cm}(\omega)}{\Theta(\omega)} \right|_{\theta} = \frac{0}{2k_1 - \omega^2 m} \quad (3-11)$$

By inspection, it can be seen that for this system, the impedance matrix Z will not contain any off-diagonal information. For an input along either degree of freedom, the transmissibility function between degrees of freedom will either evaluate to 0 or be undefined. Therefore, for a symmetrical pipe cross-section, the two degrees of freedom are uncoupled.

Corrosion is fundamentally a mass-transfer process that has been shown to be non-axisymmetric in areas where flow changes direction [28], [29]. For a simple lumped-parameter

example, the total distributed mass transfer due to corrosion will be idealized as a net point mass applied on the inner diameter of the pipe section of interest.

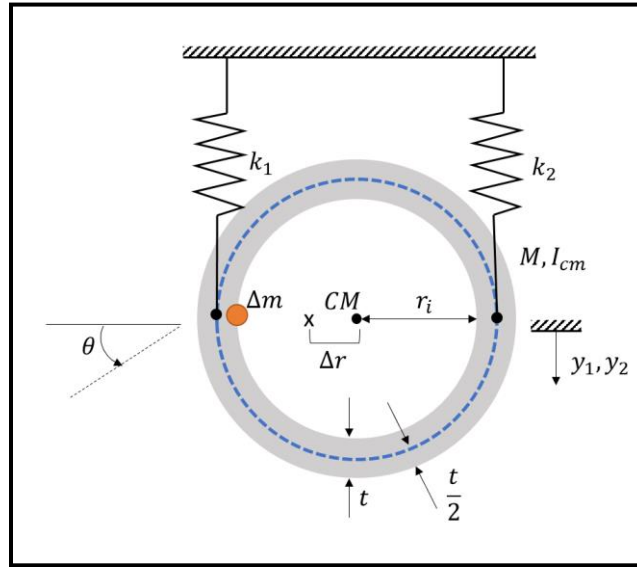


Figure 3-2: Pipe cross-section with non-axisymmetric damage

The equations of motion can be derived again, noting that the center of mass, represented by the x in Figure 3-2, no longer sits at the axis of vertical symmetry of the pipe. Note that the translational motion is defined with respect to the new center of mass and that the springs k_1 and k_2 are still assumed equivalent. Also note that $\Delta r = r_i \frac{\Delta m}{M}$, which corresponds to the distance by which the center of mass moved. Additionally, it is understood that $I_{x,M} = I_{cm} + M\Delta r^2$ and $I_{x,\Delta m} = \Delta m(r_i - \Delta r)^2$.

$$\begin{bmatrix} M + \Delta m & 0 \\ 0 & I_{x,M} + I_{x,\Delta m} \end{bmatrix} \begin{Bmatrix} \ddot{y}_x \\ \ddot{\theta} \end{Bmatrix} + k_1 \begin{bmatrix} 2 & -2\Delta r \\ -2\Delta r & 2(r_0^2 + \Delta r^2) \end{bmatrix} \begin{Bmatrix} y_x \\ \theta \end{Bmatrix} = 0 \quad (3-12)$$

These equations of motion give rise to the forced impedance matrix:

$$Z = [-\omega^2 \underline{M} + \underline{k}] = \begin{bmatrix} 2k_1 - \omega^2(M + \Delta m) & -2\Delta r k_1 \\ -2\Delta r k_1 & 2k_1(r_0^2 + \Delta r^2) - \omega^2(I_{x,M} + I_{x,\Delta m}) \end{bmatrix} \quad (3-13)$$

The subsequent transfer function matrix is given by the inverse of the impedance matrix:

$$H = Z^{-1} = \begin{bmatrix} 2k_1(r_0^2 + \Delta r^2) - \omega^2(I_{x,M} + I_{x,\Delta m}) & 2\Delta r k_1 \\ 2\Delta r k_1 & 2k_1 - \omega^2(M + \Delta m) \end{bmatrix} \quad (3-14)$$

Therefore, the transmissibility functions between degrees of freedom are given by:

$$\left. \frac{\Theta(\omega)}{Y_c(\omega)} \right|_{y_{cm}} = \frac{(2k_1 r_i) \frac{\Delta m}{M}}{2k_1(r_0^2 + \Delta r^2) - \omega^2(I_{x,M} + I_{x,\Delta m})} \quad (3-15)$$

Similarly,

$$\left. \frac{Y_c(\omega)}{\Theta(\omega)} \right|_{\theta} = \frac{(2k_1 r_i) \frac{\Delta m}{M}}{2k_1 - \omega^2 M \left(1 + \frac{\Delta m}{M}\right)} \quad (3-16)$$

This simple model suggests that the mass imbalance on the inner diameter of a pipe cross-section will cause a coupling between the rotational and translational degrees of freedom of the cross-section where this degradation occurs. Note that the Δm term can be either positive or negative, with negative Δm corresponding more closely to changes due to corrosion.

In an actual pipe segment, this cross-sectional model can be visualized as shown in Figure 3-3, where the vertical motion of the cross-section is caused by bending modes of vibration and the torsional motion of the cross-section is caused by torsional modes of vibration.

The frequency range of interest is determined by the natural frequencies of torsional and bending motion in the pipe.

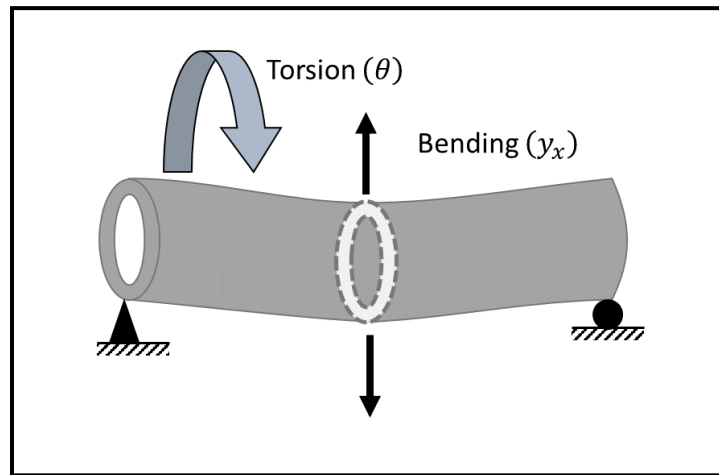


Figure 3-3: Diagram of pipe section with labeled flexing-body motions

3.2 Overview of Testing Rig

The testing rig used for Chapter 3 was composed of a tank with a heating element, a pump, and a network of pipes that fed back into the tank intake. The pump was driven by a VFD motor controller, and manual ball valves were used to control flow patterns in the pipe network. The pipe network was constructed with welded schedule 80 carbon steel pipes, bolted together at flange locations. Figure 3-4 gives an overview of the pipe network used in this research.

Unless otherwise noted, the data reported in this thesis were all taken with the water at an equilibrium operating temperature of $80 \pm 2^\circ\text{C}$ and the pipe surface at $72 \pm 2^\circ\text{C}$. Temperature was held constant with a heating element to improve the quality of operating data collected. The water temperature was measured with a resistance temperature detector probe in the tank, and the pipe surface temperature was measured with a Milwaukee handheld infrared thermometer.

The test bed was designed with two removable flanged fittings: a pipe elbow and pipe tee. The fittings were made removable so that studies of mass removal could be conducted, fittings could be replaced as needed, and so that the test bed provided flexibility. The pipe elbow fitting was the focus of this research. The 100 mV/g triaxial accelerometers used to collect vibration data and are shown in Figure 3-5, mounted on one of the pipe elbow fittings. These triaxial accelerometers were used to collect experimental and operational modal analysis response data.

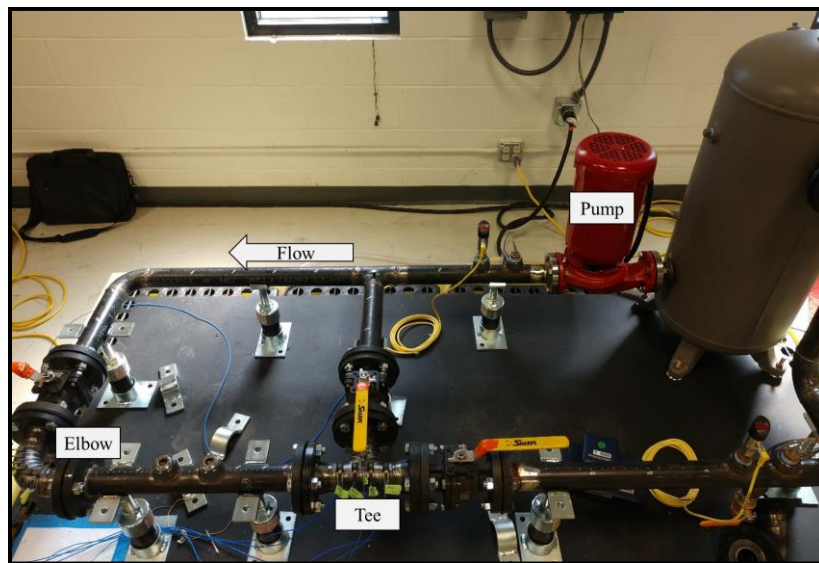


Figure 3-4: Overview image of testing rig.

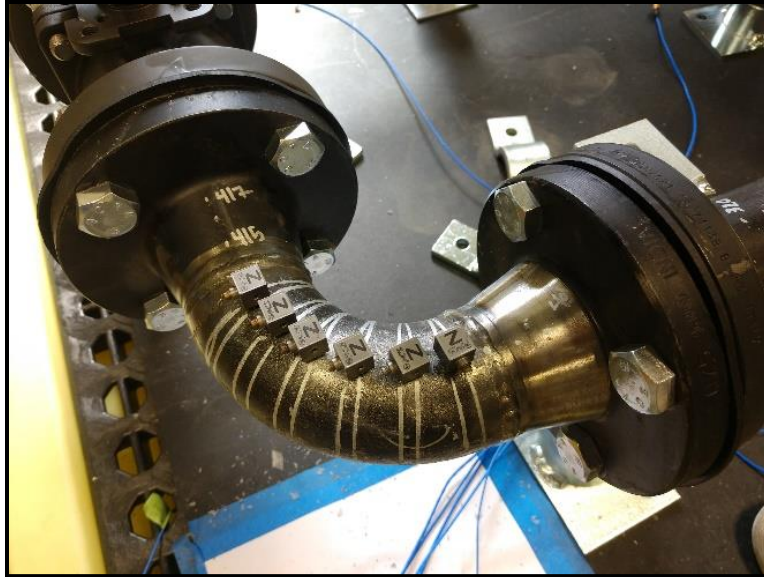


Figure 3-5: Pipe elbow shown with accelerometers mounted

3.3 Elbow Mode Shape Visualization with Experimental Modal Analysis

Recall from Section 3.1 that non-axisymmetric mass transfer was shown to cause modal coupling between bending and torsional modes in a two degree of freedom model of a pipe cross section. For this model to hold relevance in an operating test bed elbow, it must be shown that the elbow modes are conducive to the modal coupling phenomena.

To verify that the pipe elbow has such modes, experimental modal analysis was conducted on a pristine (i.e. undamaged) pipe elbow to visualize the mode shapes. Modal hammer impacts at other locations on the pipe network were used as the input forces, and the 6 triaxial accelerometers mounted on the pipe elbow were used to measure the response along the elbow. The impulse-like input to the system provides a relatively even frequency content across the frequencies studied. Figure 3-6 illustrates an example average input power spectrum used for experimental modal analysis. The important detail is that it contains relatively even frequency content so it can be used to estimate frequency response across all frequencies of interest.

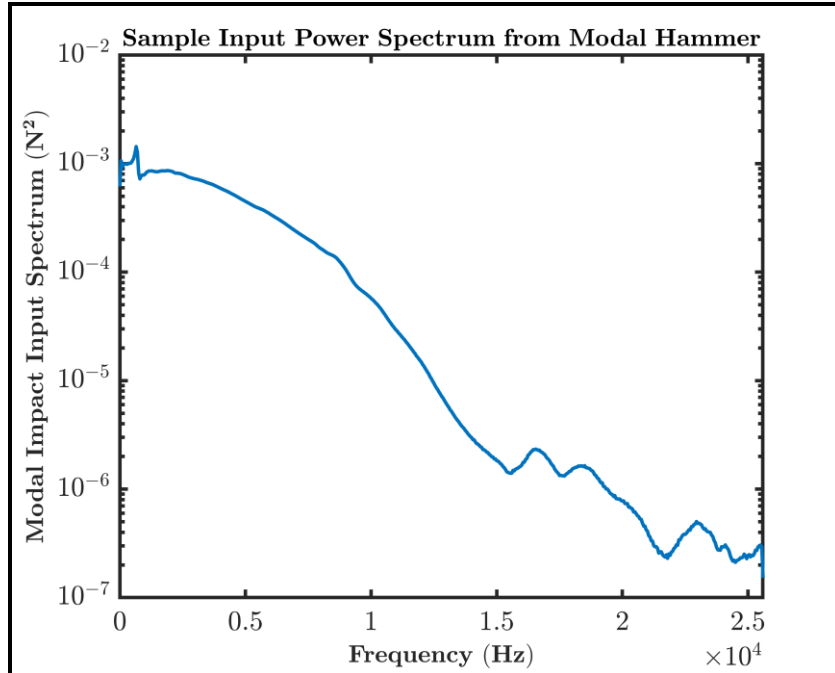


Figure 3-6: Sample average input power spectrum from modal hammer used on test bed

The relative shapes of experimentally measured modes were obtained by evaluating the imaginary component of each frequency response function at a chosen peak frequency. This component is referred to as the quadrature component. If the system is proportionally damped, the frequency response function is purely imaginary at the undamped natural frequency and the value of the frequency response function is the relative motion of the corresponding degree of freedom for that mode shape. These frequency response function components can be superimposed in the x, y, and z directions and scaled by a time-varying sinusoidal function to achieve a 3-D rendering of the experimentally measured mode shapes at a given natural frequency. One of the easiest ways to visualize these modes is with animation, but stationary plots also yield insights into the mode of vibration.

The frequency range between roughly 10 kHz and 15 kHz exhibited the bending-torsional modes represented in Figure 3-7.

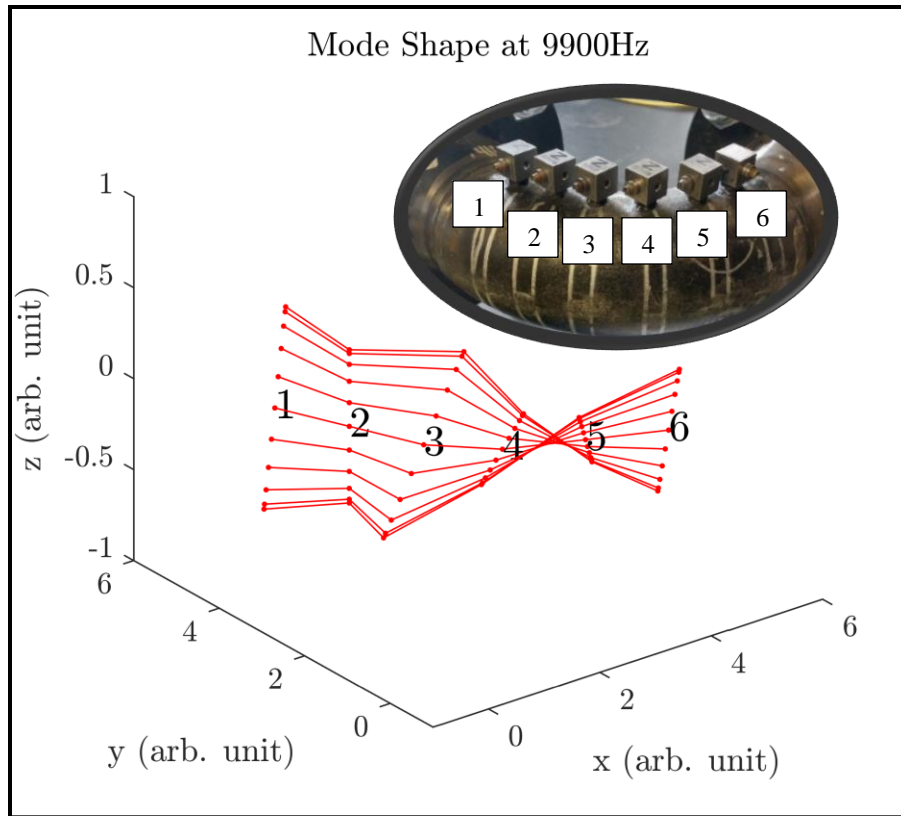


Figure 3-7: Mode shape visualization of elbow at 9900 Hz with home view shows torsion motion between accelerometers 4 and 5

In Figure 3-7, it can be seen that a torsional motion occurs between accelerometers 4 and 5. With a top-down view of the mode shape as shown in Figure 3-8, a similar torsional-bending mode can be identified near accelerometer 2. This finding indicates that at these frequency ranges, potential for bending-torsional modal coupling exists that can be examined for damage detection.

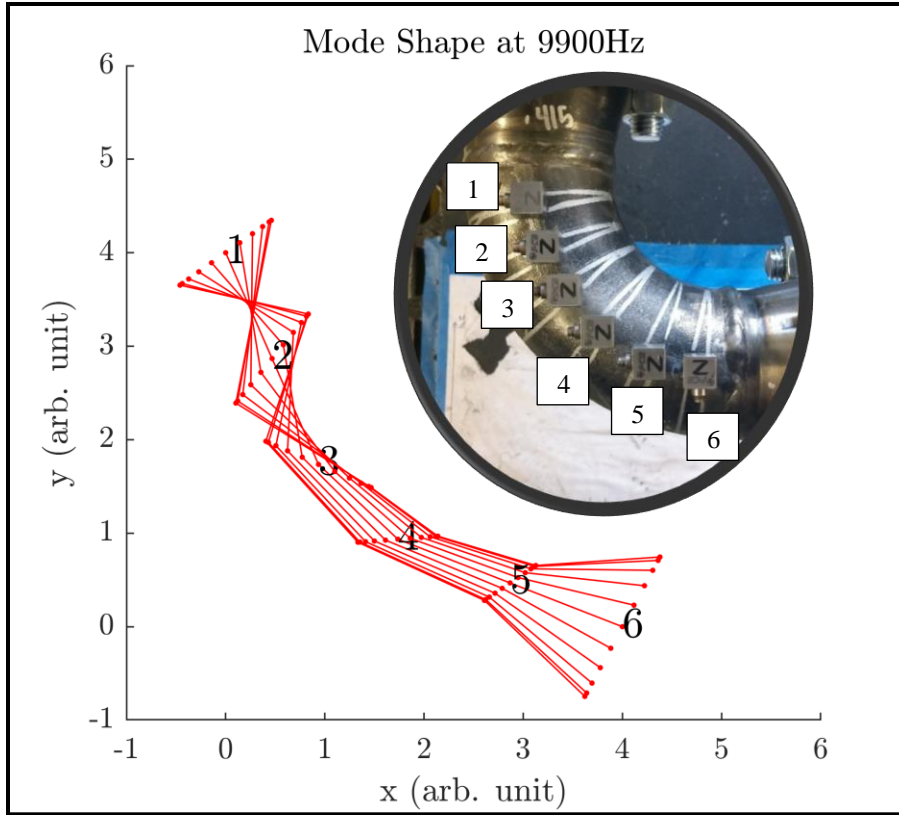
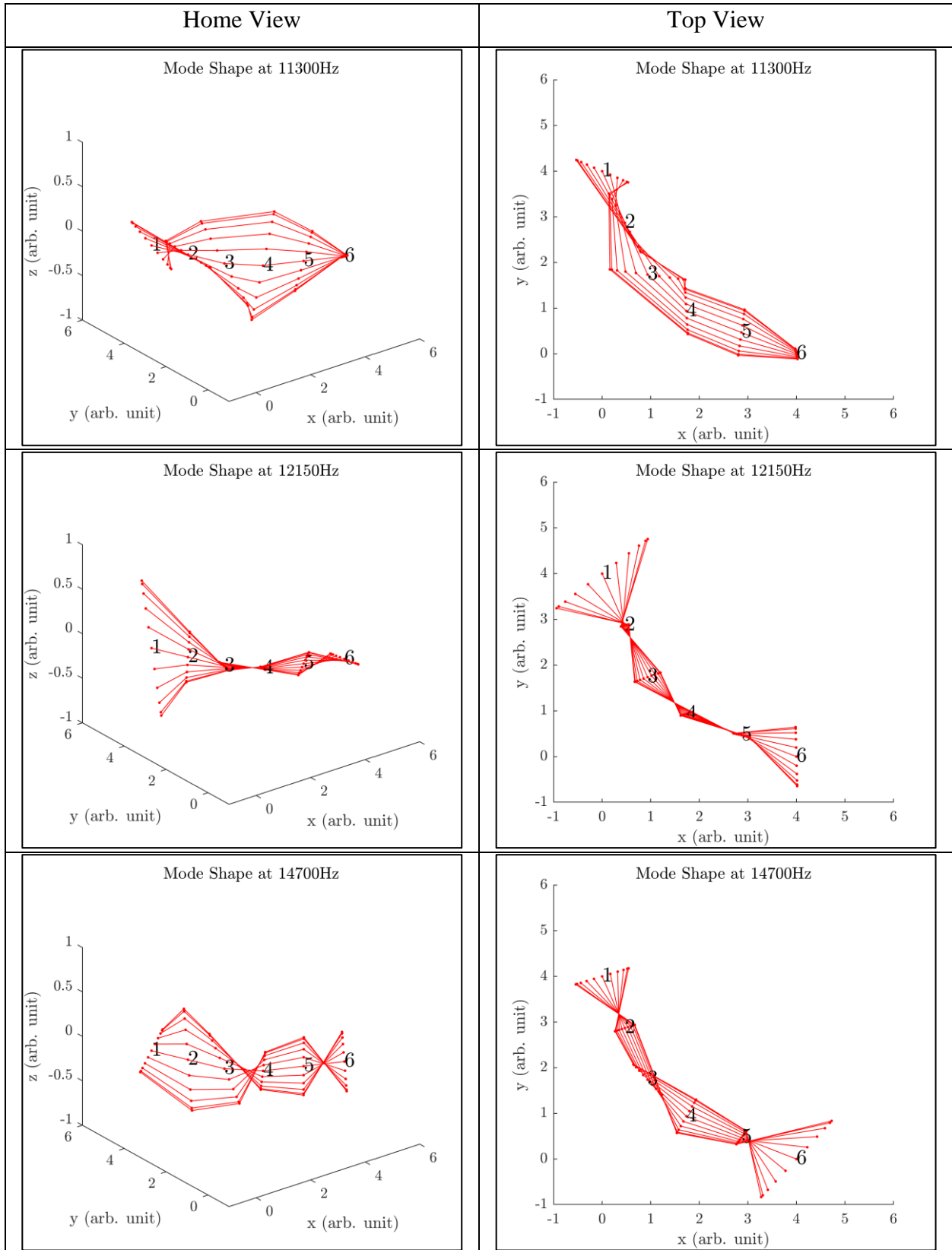


Figure 3-8: Mode shape visualization of elbow at 9900 Hz with top view shows torsional motion near accelerometer 2, indicating potential for observation of bending-torsion modal coupling

This visualization method was repeated for modes at higher frequencies. Table 3-1 summarizes these mode shapes. These visualizations indicate that there are bending-torsion resonances due to a modal impulse-like input into the pipe network. It will be shown that if the forcing input from flow and pump excitations also excite these modes, then transmissibility function estimations between bending and torsional modes of vibration will be able to detect mass change in the pipe elbow.

Table 3-1: Additional mode shapes identified with torsional-bending characteristics



The results of mode shape visualization suggest that if the transmissibility between torsional and bending modes of the pipe elbow become coupled due to non-axisymmetric mass change in the elbow, then the transmissibility functions should detect these changes in roughly the 10-15 kHz range of response. The greatest change in response was expected near accelerometers 2, 4, and 5 because the most bending-torsional motion was observed in the measurement degrees of freedom corresponding to these accelerometer locations for the above-reproduced modes.

3.4 Mass Change Detection Using Transmissibility Function Estimation

The previously discussed concept of transmissibility between degrees of freedom was applied to operating test bed data collected on the flanged pipe elbow fitting. The pipe fitting was instrumented for this experiment as shown in Figure 3-9.

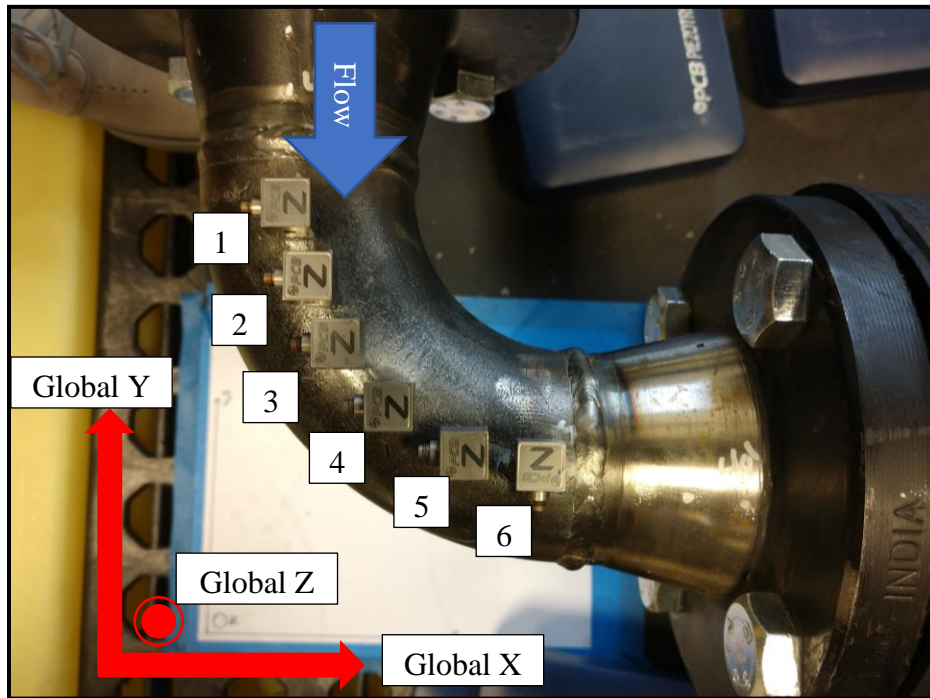


Figure 3-9: Pipe elbow with 6 triaxial accelerometers

The accelerometers were arranged within a global coordinate system to simplify data collection and organization. For all trials in this section, the variable frequency drive (VFD) motor

controller was set to 60 Hz and the test bed water was heated to an equilibrium temperature of 80°C. Volumetric flowrate data were not collected in this research, but the 5 hp pump was run at the same setting for all tests to ensure consistent flowrate was achieved.

With the motor controller operating at 60 Hz VFD input, response data were taken from the triaxial accelerometers. The auto power spectra of each response time history were calculated. The axial and torsional components of the x and y spectra were combined to achieve the axial and torsional spectra corresponding to each accelerometer location. These spectra were used to estimate transmissibility functions.

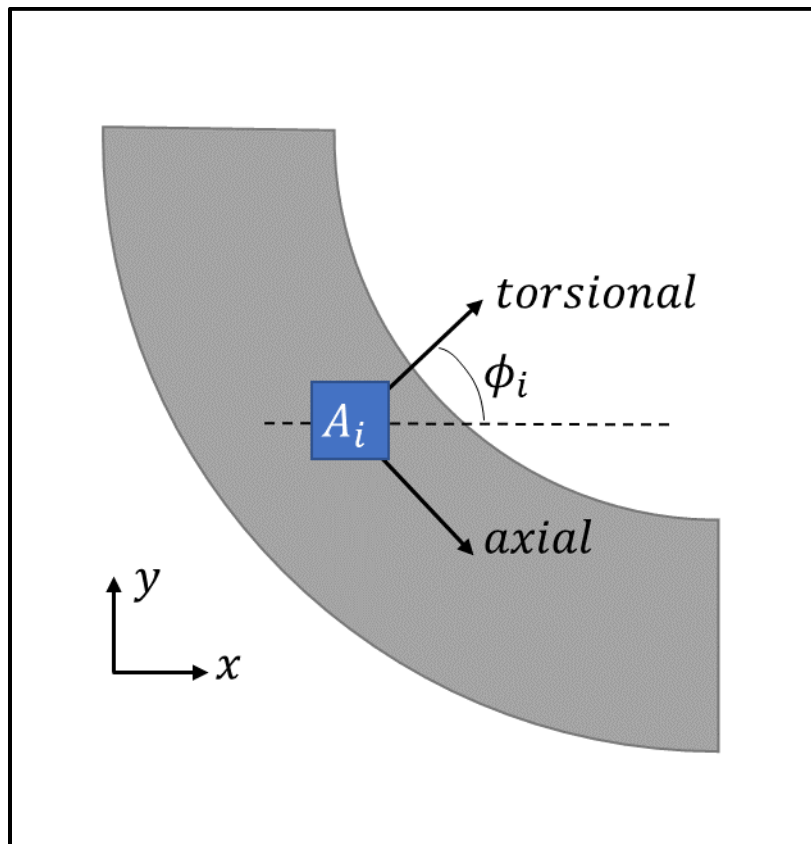


Figure 3-10: Diagram of accelerometer on elbow with given angle offset from global x-direction

The torsional (θ) component of the i^{th} accelerometer's response power spectrum was calculated with

$$G_{xx,\theta}(\omega)_i = G_{xx,x}(\omega)_i \cos(\phi_i) + G_{xx,y}(\omega)_i \cos(90^\circ - \phi) \quad (3-17)$$

where it is understood that ϕ_i is the angle offset between the global x -axis and the local axis of torsional motion on which the accelerometer is mounted. Similarly, the axial component of the accelerometer's response power spectrum was calculated with

$$G_{xx,ax}(\omega)_i = G_{xx,x}(\omega)_i \cos(90^\circ - \phi_i) - G_{xx,y}(\omega)_i \cos(\phi) \quad (3-18)$$

It can also be noted that the vertical 'bending' spectrum was identical to the global z direction spectrum because of how the accelerometers were arranged on the elbow. In line with the model developed, the elbow response was analyzed as a string of two degree of freedom systems, each corresponding to an accelerometer. The transmissibility function between the vertical bending (z) and torsional motion (θ) for the i^{th} accelerometer was calculated with

$$T(\omega)_{z_i \rightarrow \theta_i} = \frac{G_{xx,\theta}(\omega)_i}{G_{xx,z}(\omega)_i} \quad (3-19)$$

Relative transmissibility can be defined broadly as the ratio of a baseline pristine (i.e. 'healthy') transmissibility function estimate to the transmissibility function estimate of a potentially damaged system [26]. In this work, the logarithm of relative transmissibility magnitude is calculated. For unchanged transmissibility, note that the relative transmissibility defined in Equation 3-20 goes to zero.

$$T_{z \rightarrow \theta}(\omega)_r = \log \left(\left| \frac{T_{z \rightarrow \theta}(\omega)}{T_{z \rightarrow \theta}(\omega)^i} \right| \right) \quad (3-20)$$

The relative transmissibility across a sensor network can be visualized with a contour plot, where the x -axis corresponds to the sensor number, the y -axis corresponds to frequency, and the color of the plot corresponds to the magnitude of relative transmissibility. Note that the log of relative transmissibility was taken to improve visualization in the contour plots.

The baseline relative transmissibility contour was calculated between two measured time histories on the elbow during operation. Because these measurements were taken at close to the same time, the random variation between measured transmissibilities was close to zero. This is a

desired baseline condition showing that – holding operating conditions constant – the measurements do not present inherent damage indication when damage is not present

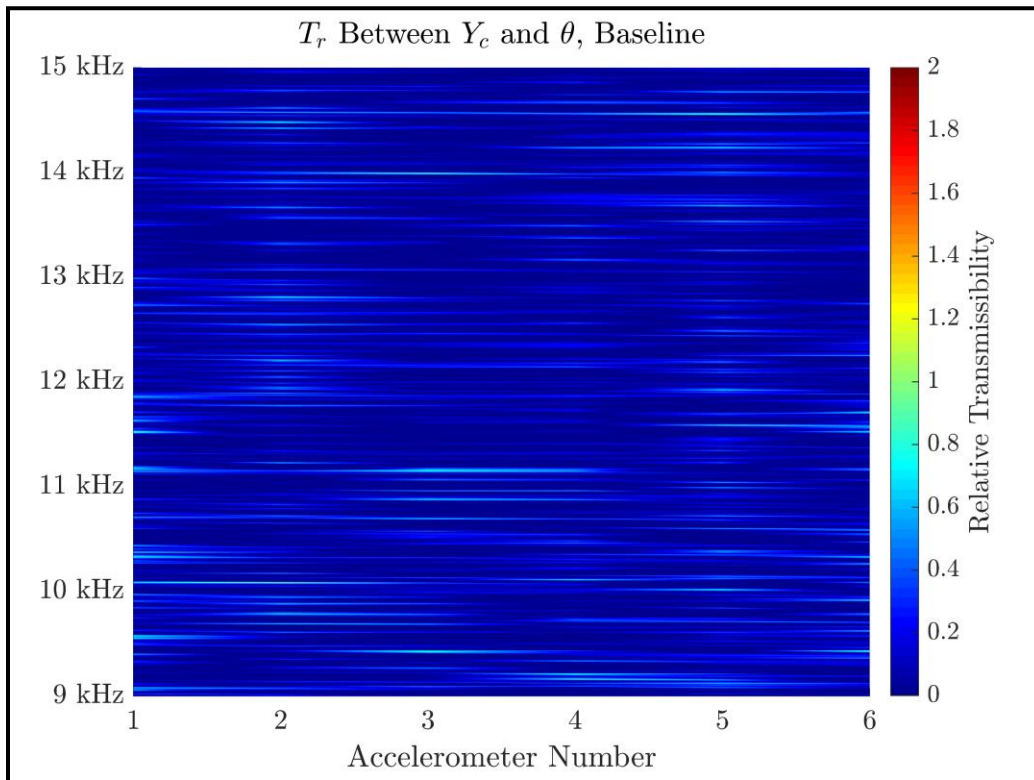


Figure 3-11: Relative transmissibility contour of baseline pipe elbow

Note here that the relative transmissibility contour is linearly interpolated between the six sensors. This visualization represents six discrete relative transmissibility vectors, but the plotting function used in MATLAB conducted a linear interpolation between each data point to create a smooth visual. The same interpolation algorithm was used for all graphs in this document.

Mass was then removed from the inner diameter of the elbow as shown in Figure 3-12 and Figure 3-13. The pipe initially weighed 6350 g. Note that the first mass reduction trial of 0.3% was performed because in the initial mass reduction stage, more material than desired was removed. This was due to operator unfamiliarity with the die grinder and was corrected to reduction within a gram of desired mass in all future mass removal trials. Table 3-2 summarizes the mass removal stages and data collection dates on the first elbow tested.

Table 3-2: Mass removal stages on pipe elbow

Trial Number	Total Mass Removed	Percent of Initial Mass Removed	Date of Removal and Test
1	19 g	0.3%	6-28-19
2	32 g	0.5%	7-01-19
3	48 g	0.75%	7-01-19
4	63 g	1%	7-05-19
5	79 g	1.25%	7-08-19
6	95 g	1.5%	7-08-19

Note in Figure 3-13 that material was only removed beyond the flange weld to preserve the integrity of the weld during testing. Figure 3-13 shows the stages of material removal on the inside of a pipe elbow, and Figure 3-15 shows the tool used to remove material.



Figure 3-12: Top view of elbow with area of mass removal shown in yellow

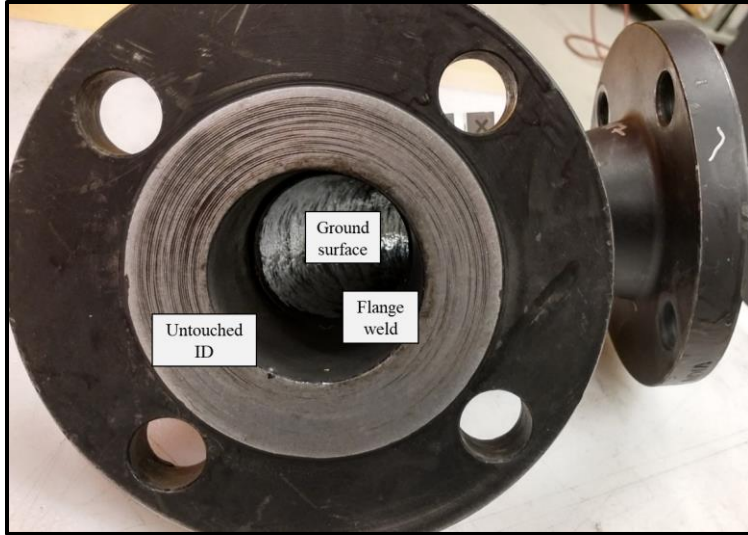


Figure 3-13: View of inner diameter of pipe elbow with material ground away



Figure 3-14: Pipe elbow before (left) during (middle) and after (right) material removal



Figure 3-15: Milwaukee 2" die grinder and carbide bit used to remove material

The removal of mass and subsequent collection of operating transmissibility data showed changes in the relative transmissibility relating to the previously observed mode shapes. Figure 3-16 through Figure 3-21 illustrate the change in relative transmissibility contour along all 6 accelerometers for the mass reduction trials performed. These figures show a broad progression of relative transmissibility with damage.

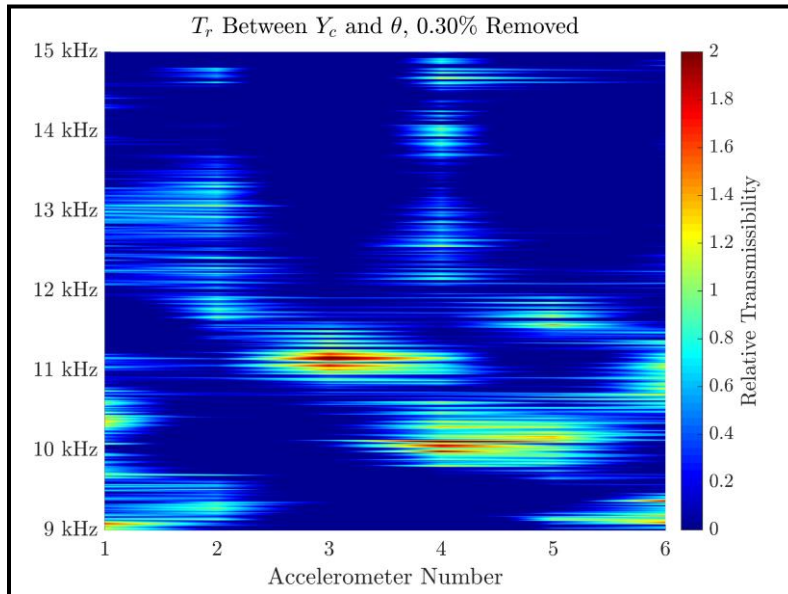


Figure 3-16: Relative transmissibility contour with 0.3% mass removed from elbow

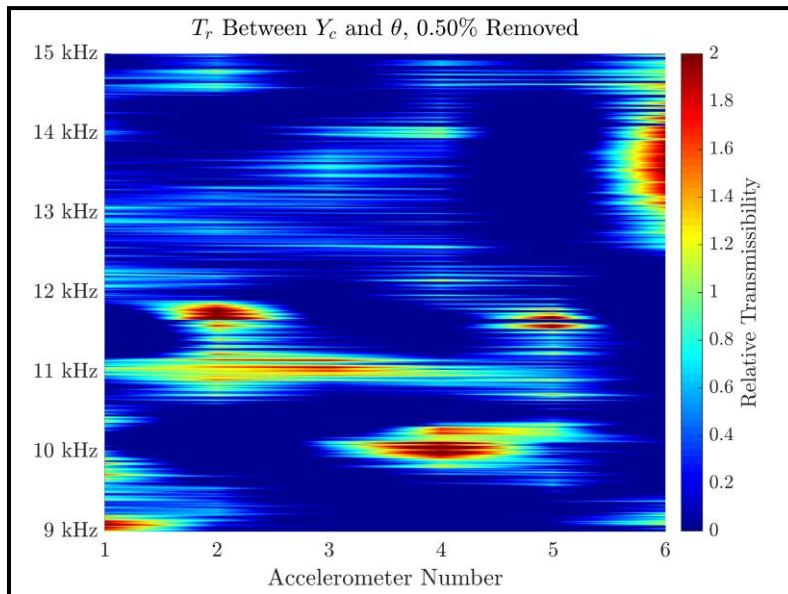


Figure 3-17: Relative transmissibility contour with 0.5% mass removed from elbow

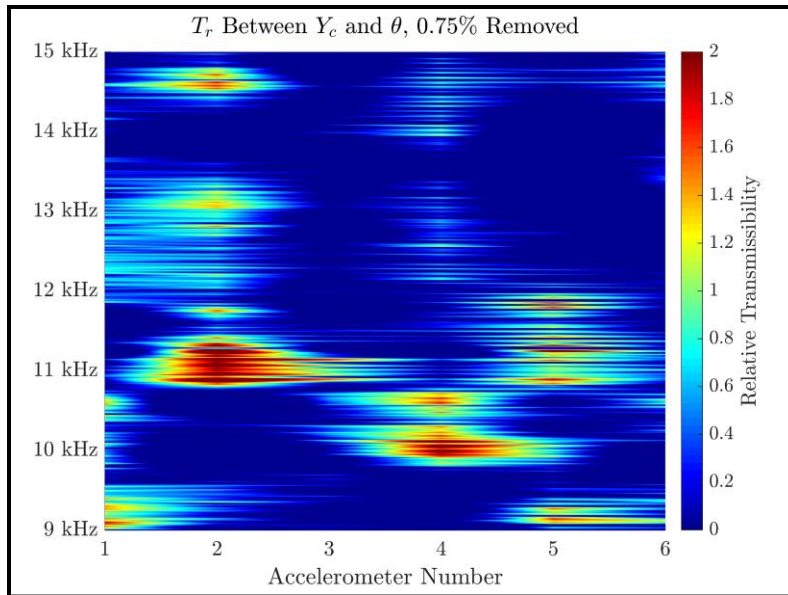


Figure 3-18: Relative transmissibility contour with 0.75% mass removed from elbow

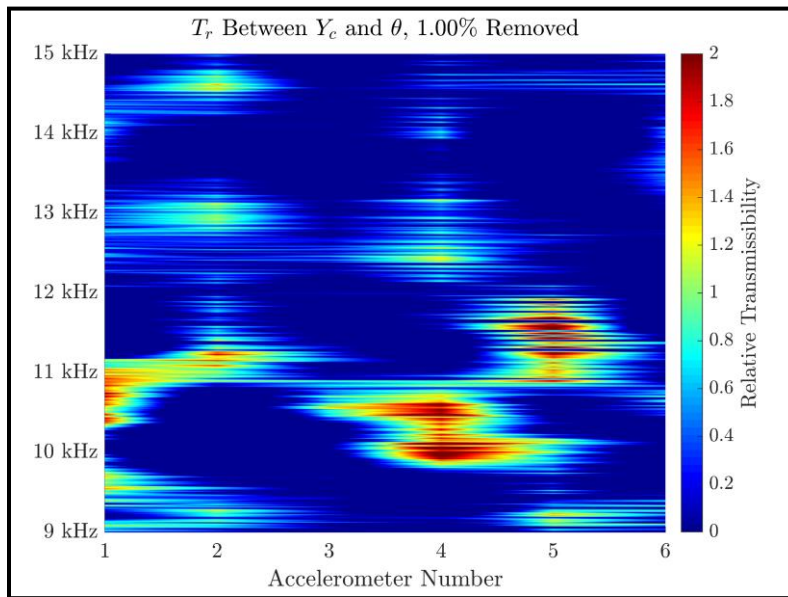


Figure 3-19: Relative transmissibility contour with 1% mass removed from elbow

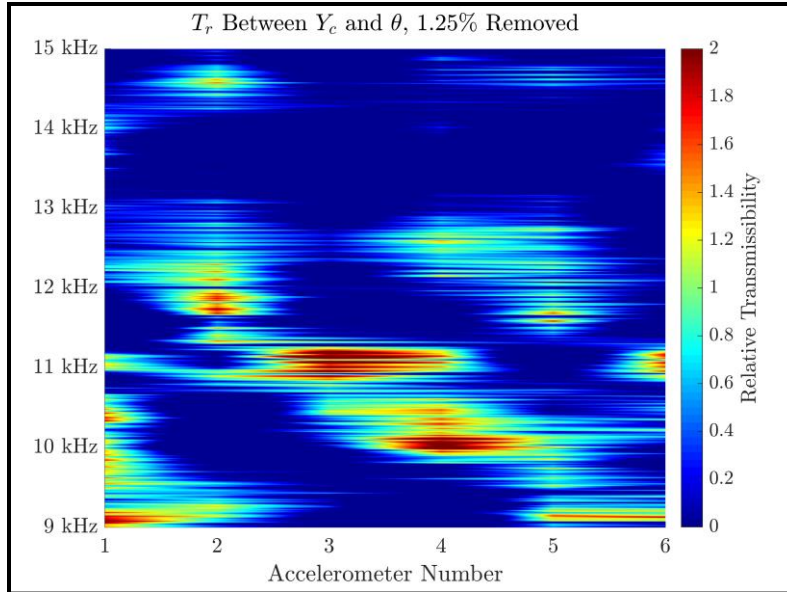


Figure 3-20: Relative transmissibility contour of elbow with 1.25% mass removed

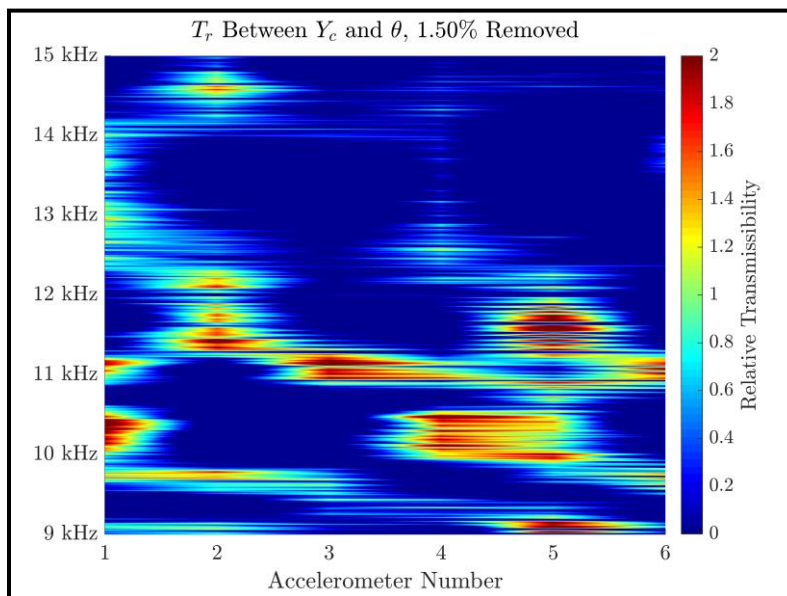


Figure 3-21: Relative transmissibility contour of elbow with 1.5% mass removed

Of note, the relative transmissibility shift observed at accelerometers 4 and 5 between the bending and torsional degrees of freedom exhibited a generally steady increase as the mass reduction in the elbow increased. The contour at accelerometer 2 did not follow a positive correlation between mass removal and relative transmissibility, indicating that although bending-torsional motion was observed in the experimental modal analysis, this sensing location was not

sensitive to damage in this analysis. Figure 3-19 summarizes this increase with the mass reduction trials performed.

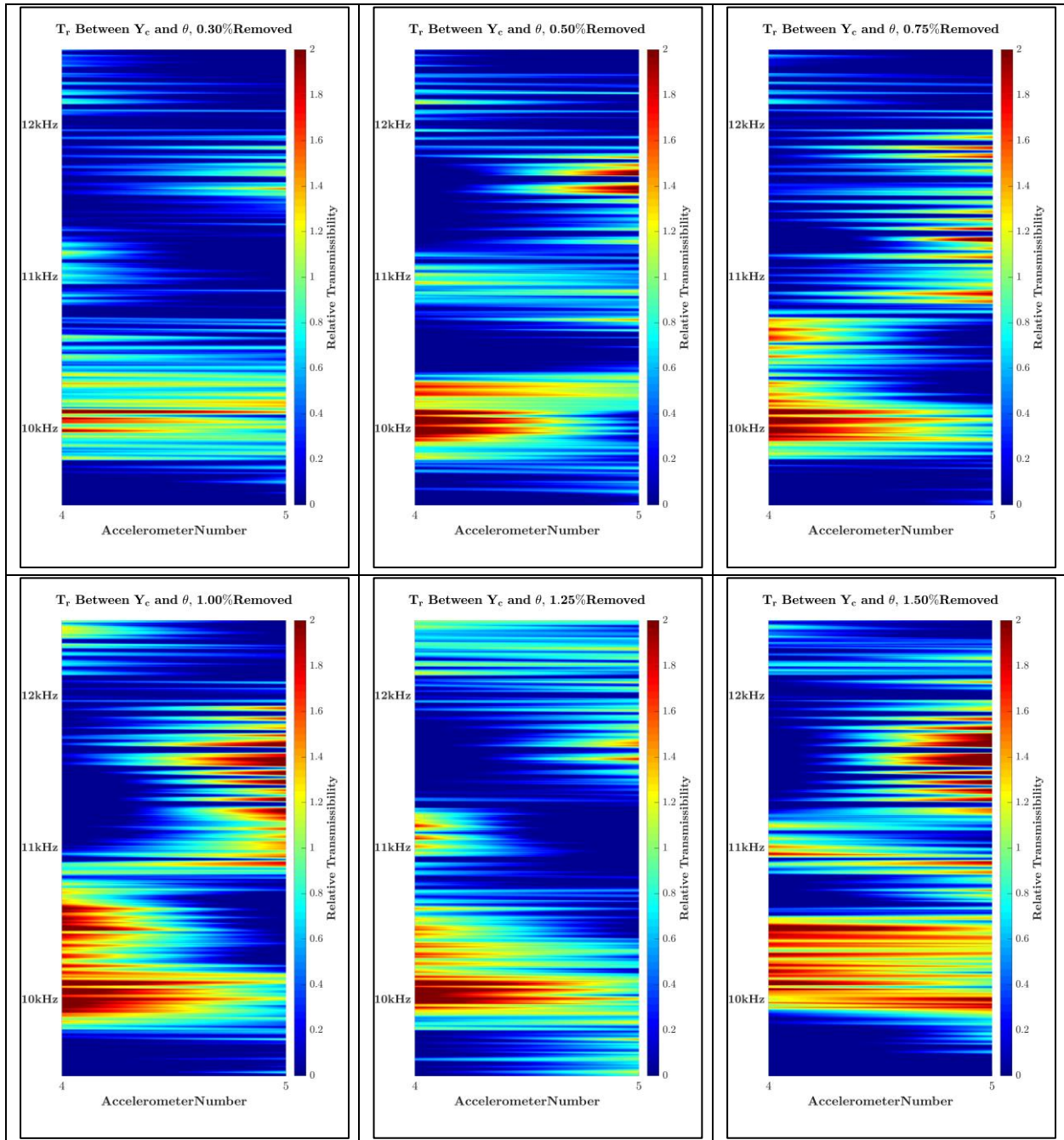


Figure 3-22: Relative transmissibility plots between accelerometers 4 and 5, 9500-12500 Hz

A damage index calculation for quantifying the change in transmissibility shifting was formulated using the weighted sum of relative transmissibility over all N measured frequencies at the i^{th} accelerometer:

$$DI_i = \sum_{k=1}^N W_i(\omega_k) T_{z \rightarrow \theta, i}(\omega_k)_r \quad (3-21)$$

Here, $W_i(\omega_k)$ is a weighting function determined by the k^{th} frequency ω_k and $T_{z \rightarrow \theta}(\omega_k)_r$ is the relative transmissibility value calculated for the k^{th} frequency

For each material removal trial conducted, 10 operating data samples were collected back-to-back. With one baseline transmissibility measurement held as the reference by which all other relative transmissibilities were calculated, Equation 3-21 was evaluated at accelerometer 4 where

$$W_4(\omega) = \begin{cases} 1, & \text{for } 10\text{kHz} \leq \omega \leq 12\text{kHz} \\ 0 & \text{otherwise} \end{cases} \quad (3-22)$$

This damage index calculation yielded 9 damage index approximations for each mass removal case. A boxplot of these damage indices is given in Figure 3-23. The damage indices calculated are given in Table 3-3.

A similar calculation was made for accelerometer 5 using the weighting function in Equation 3-23. This led to the boxplot shown in Figure 3-25 and the damage indices given in Table 3-4.

$$W_5(\omega) = \begin{cases} 1, & \text{for } 10\text{kHz} \leq \omega \leq 12\text{kHz} \\ 0 & \text{otherwise} \end{cases} \quad (3-23)$$

Figure 3-23 and Figure 3-24 indicate that the damage index can be correlated with the degree of mass change in a pipe elbow. Additionally, the method of analysis used did not require multiple sensors, but rather a single sensor with multiple directions of sensitivity for each location of interest.

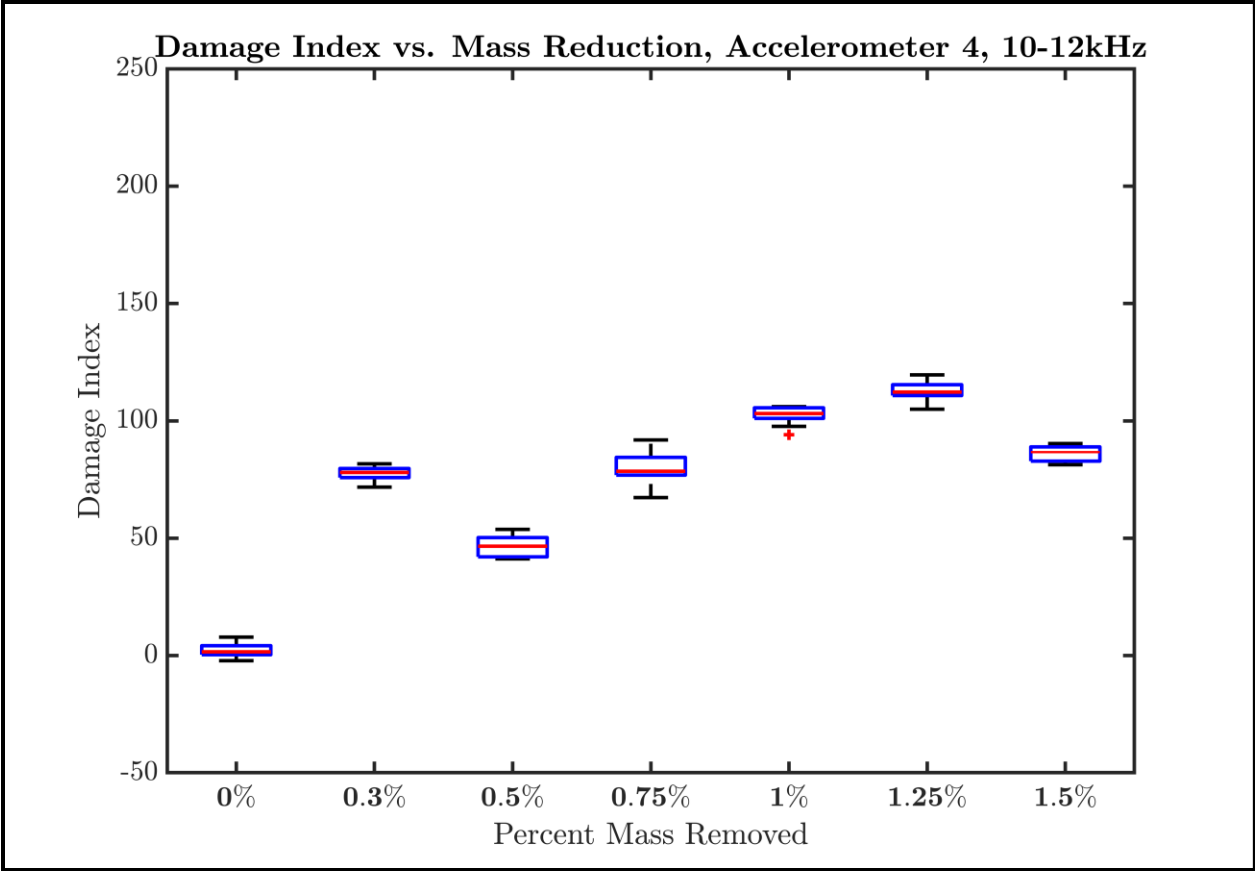


Figure 3-23: Boxplot of damage index vs percent mass removed on elbow at accelerometer 4

Table 3-3: Damage indices calculated at accelerometer 4 for each mass removal trial, 10-12 kHz

Trial	Baseline	0.30%	0.50%	0.75%	1.00%	1.25%	1.50%
1	0	82	49	76	102	120	81
2	4	79	44	83	94	111	90
3	6	78	42	80	106	118	88
4	-2	74	42	77	105	109	86
5	8	80	47	88	105	112	81
6	2	72	49	78	103	105	83
7	0	78	54	67	98	114	88
8	1	77	41	92	103	115	90
9	2	78	54	79	106	112	83

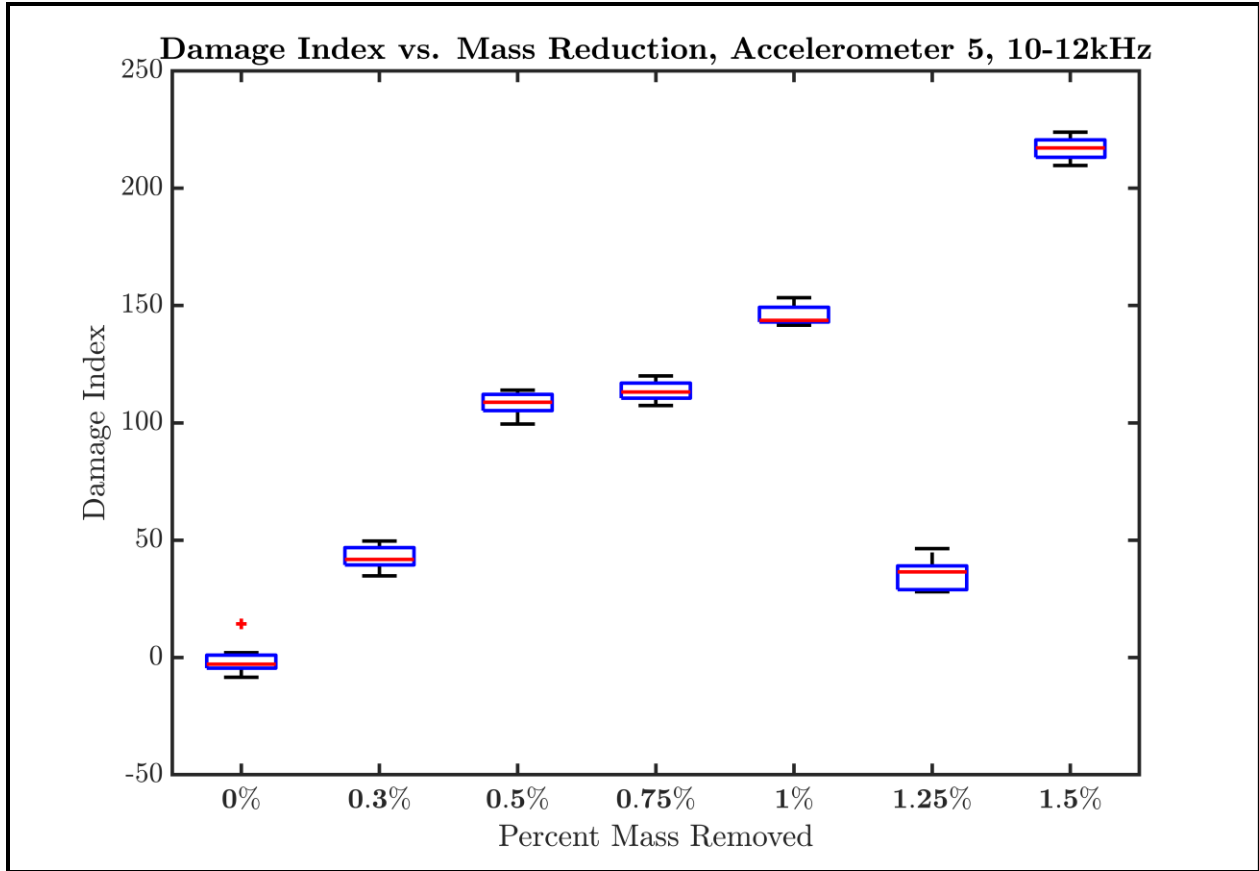


Figure 3-24: Damage index vs percent mass removed at accelerometer 5

Table 3-4: Damage indices calculated at accelerometer 5 for each mass removal trial, 10-12 kHz

Trial	Baseline	0.30%	0.50%	0.75%	1.00%	1.25%	1.50%
1	-4	50	112	112	143	39	213
2	14	35	109	109	143	37	213
3	-8	42	107	107	148	28	224
4	-4	39	100	117	151	37	217
5	-2	47	108	120	144	29	223
6	-3	42	114	111	143	28	210
7	2	42	110	114	142	41	216
8	1	39	101	113	149	31	217
9	-6	47	113	118	153	46	220

3.5 Variability Between Elbow Removals and Reinstallations

Recalling Figure 3-23 and Figure 3-24, data from the 1.25% mass removal trial did not match the trends seen in the rest of the data. Particularly in Figure 3-24, this dataset appeared to be an interruption in the otherwise clear trend between amount of mass change and damage index.

Between the 1% and 1.25% mass removal trials, the tank heating element was mistakenly left on while the mass was ground away from the pipe elbow. Because the tank was closed off from the pipe circuit, the heating element caused the gauge on the tank to overpressure and the water temperature in the tank to exceed 115°C. It was hypothesized that circulating this hot, pressurized water may have affected the boundary conditions on the elbow fitting by deteriorating the rubber gaskets used to seal this pipe connection. It was also hypothesized that the elbow was installed incorrectly and that bolts may have been left loose, causing a change in boundary condition and thus relative transmissibility compared to the correctly installed baseline measurement configuration.

The loose-installation hypothesis was tested by taking three transmissibility measurements on the operating elbow. Between each measurement, the elbow was fully removed from the test bed before being re-installed and tightened down completely. After this collection was used to establish variability between correct installations, one bolt on each side of the elbow was loosened slightly and the data were re-collected a fourth time. Finally, the loose bolts were re-tightened and a seventh dataset was collected on the elbow to verify that any changes occurred because of the loose bolts on the elbow.

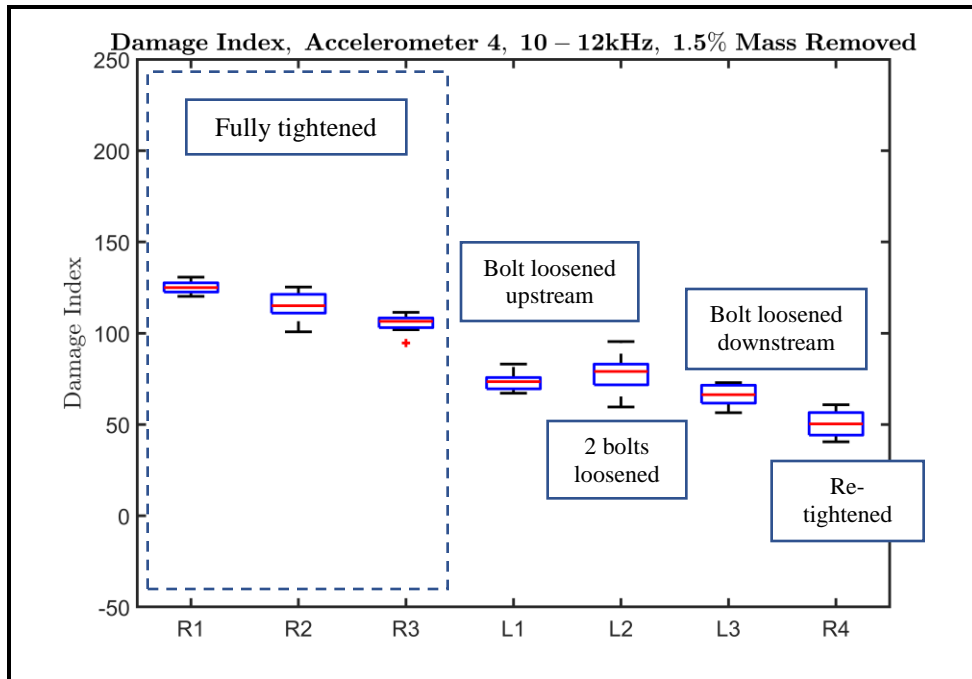


Figure 3-25: Accelerometer 4 damage index boxplots for elbow removal variability trial, 1.5% mass reduction

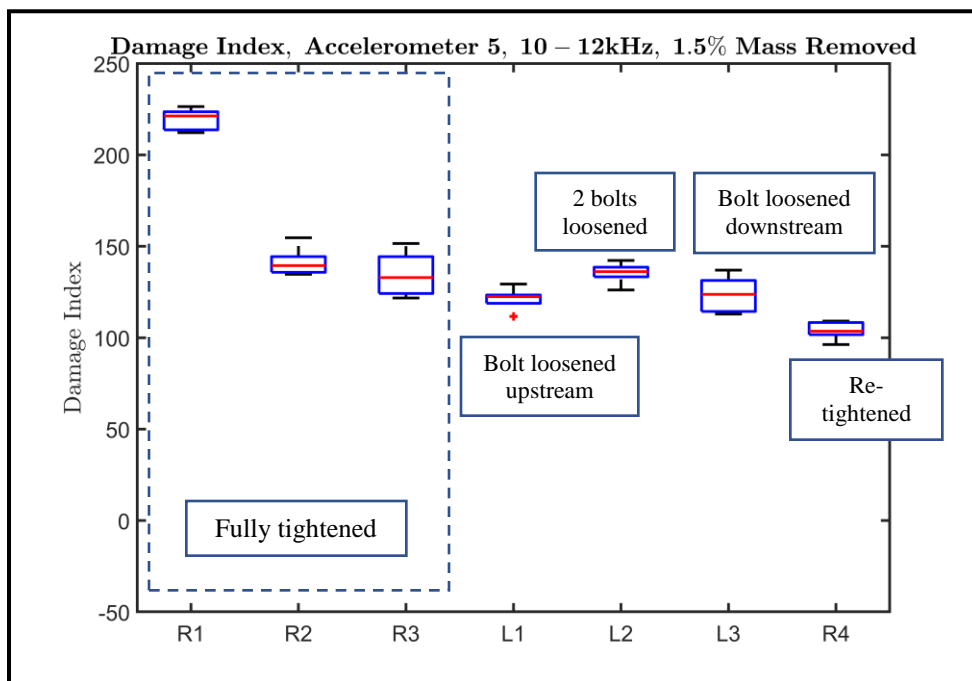


Figure 3-26: Accelerometer 5 damage index boxplots for elbow removal variability trial, 1.5% mass reduction

In trial L1, a bolt on the upstream side of the elbow was loosened slightly. In trial L2, another bolt on the downstream side of the elbow was loosened. In trial L3, the loosened bolt from trial L1 was re-tightened. In trial R4, the last remaining loosened bolt was re-tightened. For safety reasons, the fluid was not pressurized during bolt-loosening.

Figure 3-25 and Figure 3-26 did not show the expected change in calculated damage index between the three normally installed elbow trials (R1 through R3), the three trials with one or more loosened bolts (L1 through L3) and the final trial in which the bolts were re-tightened (R4). Instead of sharply decreasing with a loosened bolt and recovering, the damage indices continued to reduce between trials, perhaps due to the continued degradation of the rubber gasket between trials.

It was noted that all data samples collected after the first bolt was loosened (L1 through R4) showed reduced damage index when compared to the first three normal installation trials. Interestingly, after the loosened bolts were all re-tightened, a further reduction in damage index was seen. All damage indices were calculated with respect to the same baseline used for Figure 3-23 and Figure 3-24.

3.6 Day-to-Day and Run-to-Run Variability in Transmissibility Function Estimation

The data analyzed in Section 3.4 did not take into account that the transmissibility functions of the test bed would be affected by day-to-day variability, cycling on and off of the pump, and sources of variability introduced by the removal and re-installation of the pipe elbow between mass reductions. Although this could be assumed based on the fact that the transmissibility function between two measurements is more sensitive to local parameter changes than it is to global parameter changes, verification that a given baseline measurement remains valid over time was sought.

To evaluate day-to-day variability in relative transmissibility damage index, the test bed was operated up to an equilibrium water temperature of $80 \pm 2^\circ\text{C}$ every day for 8 days. At 2:00 PM every afternoon during this period, baseline operating data were collected on the first healthy pipe elbow with no modifications (i.e. no mass was removed, added, etc.). Between each data collection cycle, the two valves upstream of the fittings were cycled closed-open, and the pump was shut completely off between data acquisition cycles. 10 samples of baseline data were

collected per-day. Relative transmissibility plots were generated between the day 1 transmissibility data and the subsequent 7 days' transmissibility data, with day 1 data held as the constant reference transmissibility for all calculations.

When these data were used to calculate damage indices for the same frequency ranges discussed in Section 3.4, the resulting damage index boxplots in Figure 3-27 and Figure 3-28 were produced.

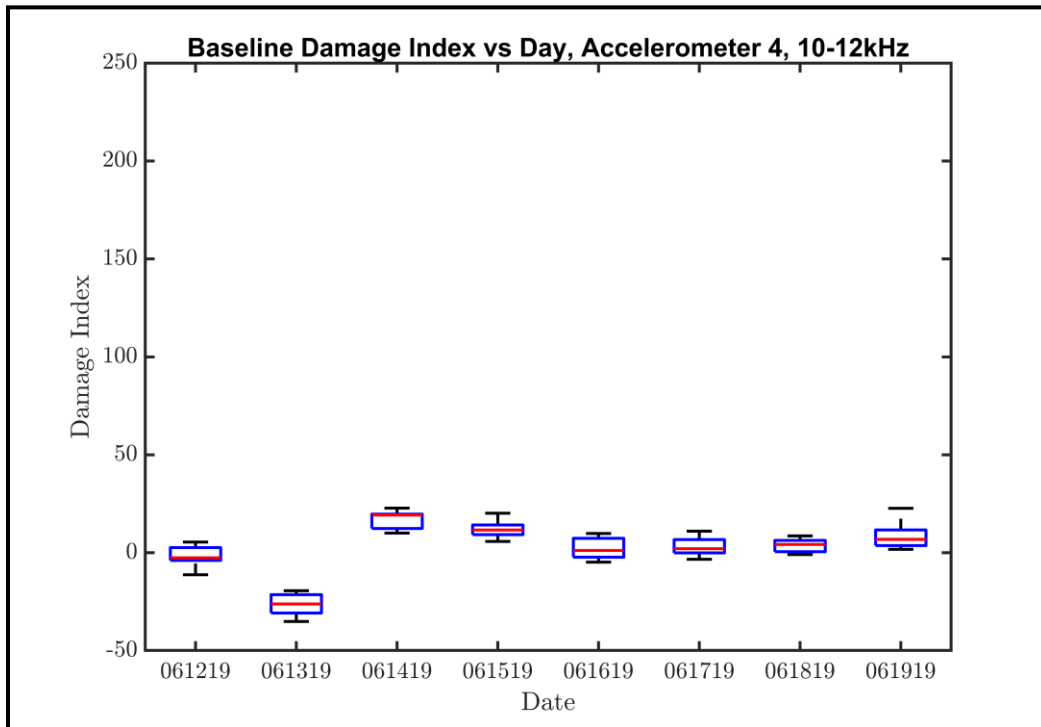


Figure 3-27: Damage index calculated at accelerometer 4 over 1 week of operation, 10-11 kHz

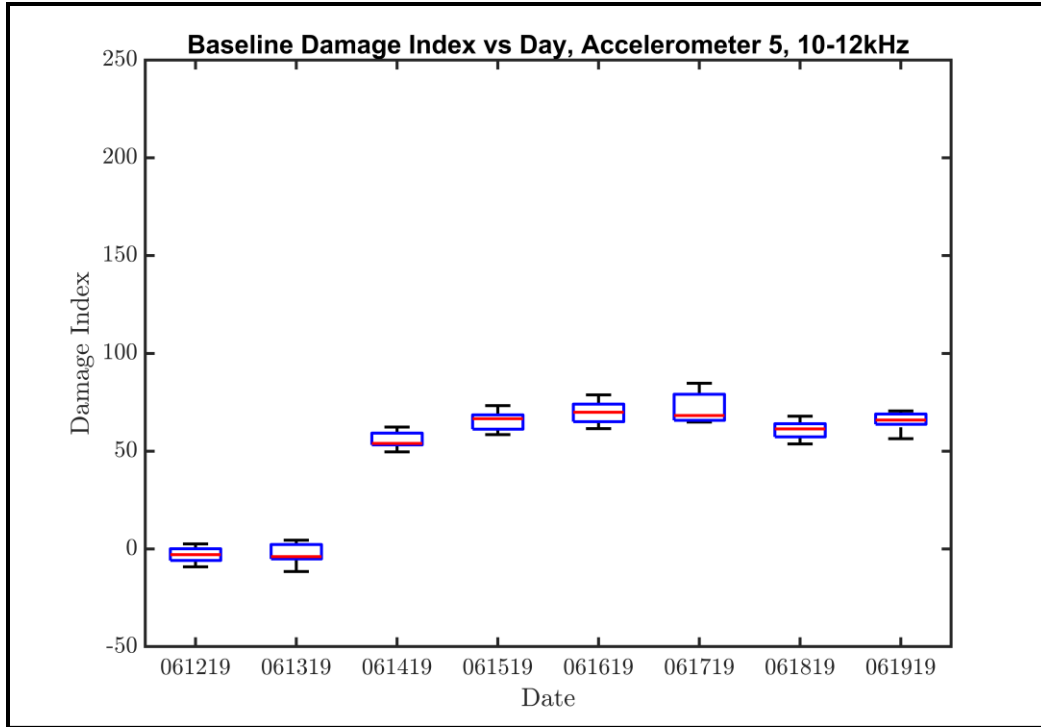


Figure 3-28: Baseline damage index calculated at accelerometer 5 over 8 days of operation, 10-12 kHz

Note that the damage index scale is the same for Figure 3-24 through Figure 3-28. These data suggest that, when accounting for only day-to-day variability in test bed transmissibility measurements, the first time at which mass transfer becomes consistently detectable by the damage index calculation method shown above is when 0.75% of the original mass of the pipe elbow has been removed. These data also show that the damage index calculation from accelerometer 4 was more robust to day-to-day variability and pipe-to-pipe variability than the damage index calculation from accelerometer 5.

3.7 Repetition of Mass Reduction Experiment

Although the anomalous results seen in the mass reduction trials are not perfectly explained by the examination of variability between elbow removal trials, it is feasible that one or multiple incorrectly installed bolts could have contributed to the change in damage index seen.

Another source of potential variability was the deteriorating rubber gaskets that were used to seal the elbow joint. Between trials, it was qualitatively noted that the gaskets continued to

deteriorate over the course of approximately two months of data collection. This is likely due to the operating temperature of the water and the repeated removal and re-installation of the gasket material. Operating pressure was also not controlled in the first iteration of the pipe elbow mass removal trials. Figure 3-29 shows the gaskets after their final removal from the test bed.



Figure 3-29: Degraded gasket after use in first mass removal experiments

The mass removal experiment was repeated on a new schedule 80 pipe elbow, nominally identical to the first elbow tested. In this experiment, operating pressure was held at 5 ± 0.5 psi and the gaskets on the elbow were replaced with new gaskets between trials. Operating temperature was kept at 80°C and other parameters were held constant. Accelerometers were attached to the elbow in the same manner as before, and the location of the elbow in the circuit was the same as before as shown in Figure 3-30.



Figure 3-30: Configuration of second elbow used in mass removal experiment

When data collection was repeated in the same way as before, the following damage indices were produced with the new pipe.

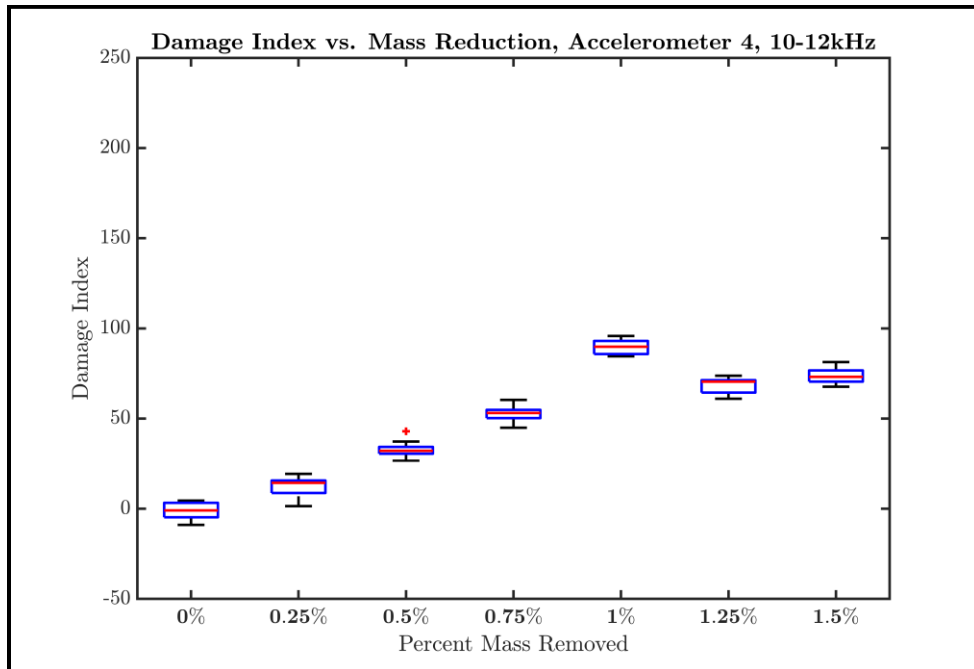


Figure 3-31: Damage index vs mass reduction for second pipe elbow, accelerometer 4

Although Figure 3-31 indicates that the trend between damage index and mass change seen in accelerometer 4 was consistent between elbows, Figure 3-32 shows that the strong trend observed in the first elbow was not seen in the second. This finding suggests that although there is potential for the use of transmissibility function estimates for damage detection, a deeper understanding of the causes for changing relative transmissibility is needed.

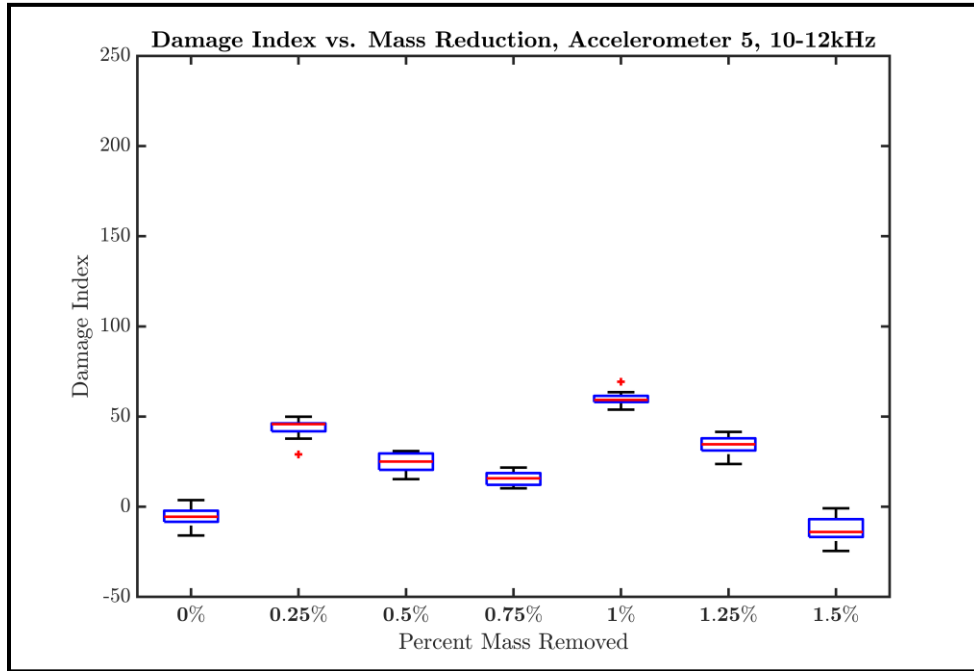


Figure 3-32: Damage index vs mass reduction for second pipe elbow, accelerometer 5

3.8 Effects of Operating Temperature and Pressure on Damage Index Calculation

As shown above, damage index variability with days of operation and between fittings was characterized. In this section, gasket material, operating temperature, and operating pressure are evaluated for their effects on the damage index.

The evolution of the damage index can be represented by the partial differential equation:

$$\Delta DI = \frac{\delta DI}{\delta x_1} \Delta x_1 + \frac{\delta DI}{\delta x_2} \Delta x_2 + \dots + \frac{\delta DI}{\delta x_n} \Delta x_n + \frac{\delta DI}{\delta D_1} \Delta D_1 + \frac{\delta DI}{\delta D_2} \Delta D_2 + \dots + \frac{\delta DI}{\delta D_m} \Delta D_m \quad (3-24)$$

Here, x_1 through x_n represent n variables that affect the damage index but which are not considered ‘damage’. D_1 through D_m are m values corresponding to real damage sustained by the pipe. To distinguish ‘non-damage’ from ‘real damage’ in the lumped damage index value, several non-damage variables were investigated for their effect on the damage index measurement.

The effect of temperature on relative transmissibility damage index was first investigated. The second elbow with a 1.5% mass reduction was installed in the test bed. The test bed was operated at 5°C steps in measured water temperature, and operating data were collected for each operating temperature. The pressure of the tank for each data collection trial was atmospheric. Damage indices were calculated with respect to a healthy baseline. This experiment was conducted twice to investigate the repeatability of effects seen on the damage index due to operating temperature. Figure 3-33 and Figure 3-34 summarize the damage index vs temperature plots produced from these two trials. Note that for an actual pipe network in a nuclear power plant, the variability of temperature is expected to be smaller than the range of temperatures tested.

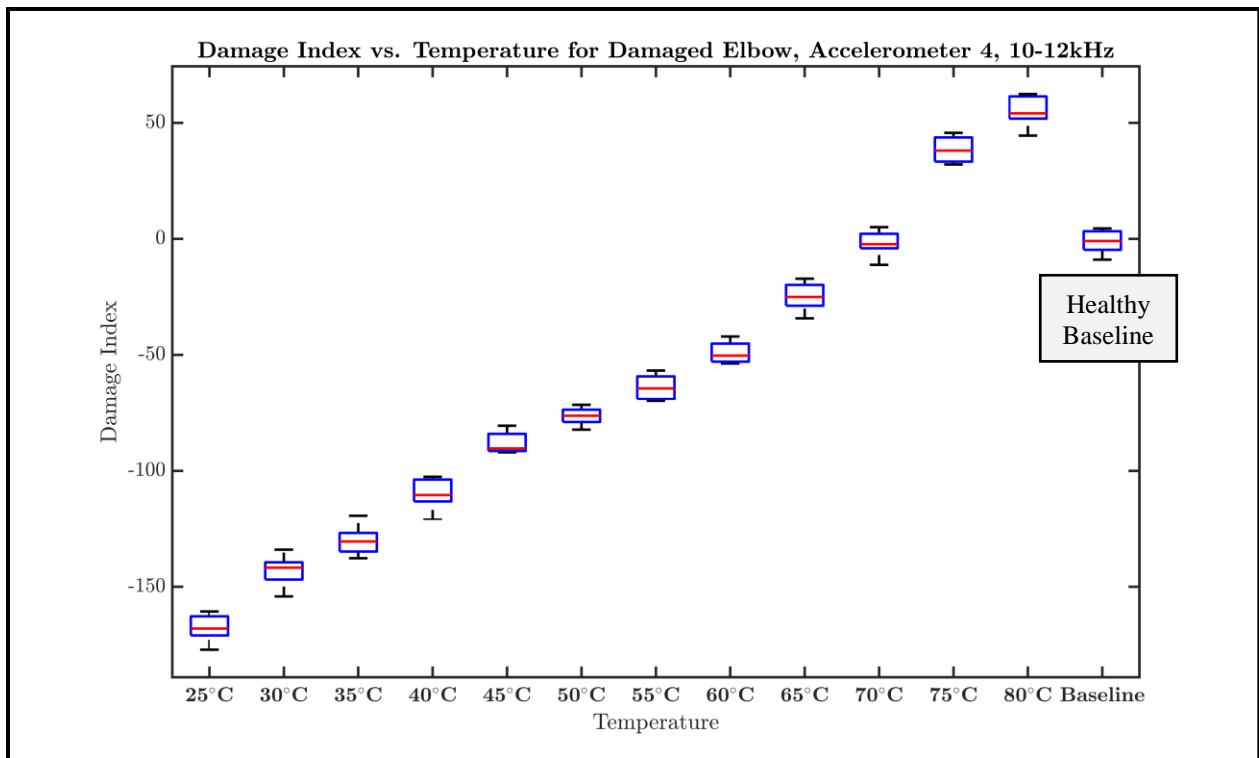


Figure 3-33: Temperature vs damage index for damaged pipe elbow mounted with EPDM rubber gaskets. Trial 1 of 2 indicates strong positive correlation between temperature and damage index

Figures 3-30 and 3-31 indicate that a strong trend was seen between temperature and damage index and that the trend was repeatable between days of operation. This study suggests that operating temperature should be accounted for when using the described relative transmissibility damage index method for estimating damage. More repetitions of this experiment would allow for an estimation of the relationship between temperature and the appropriate scaling factor to be applied to the damage index estimation.

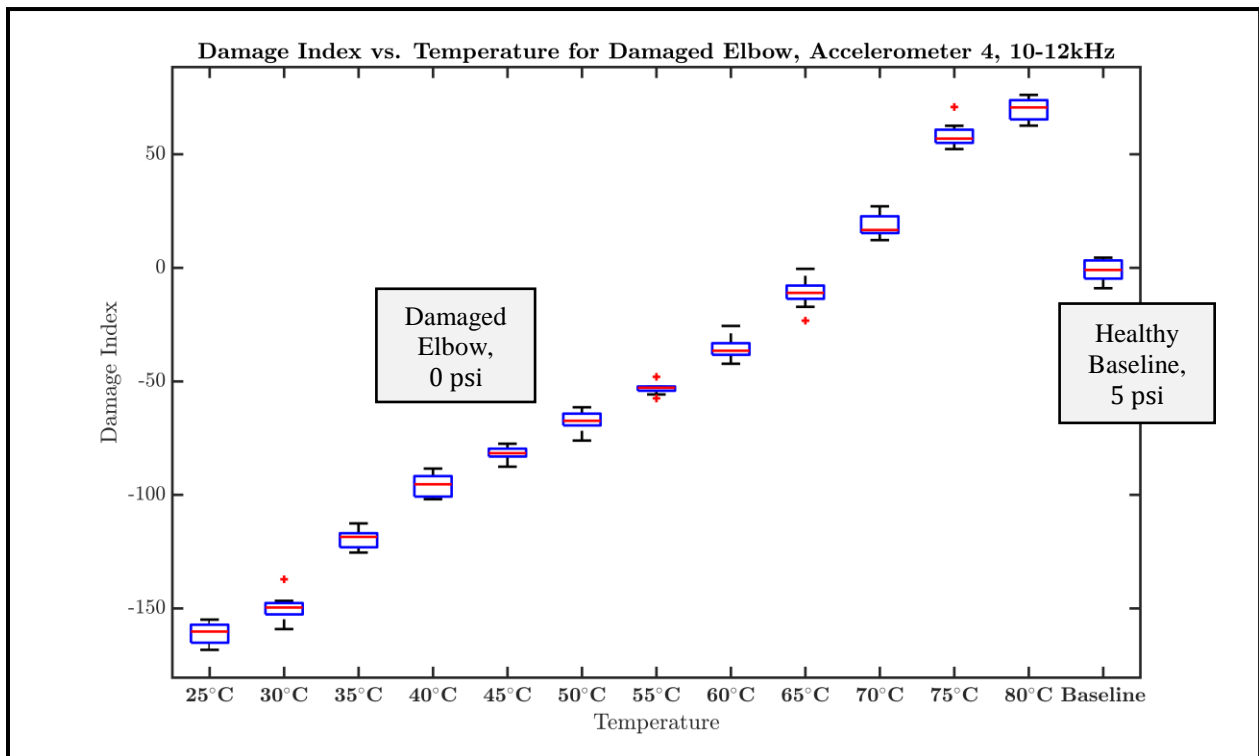


Figure 3-34: Temperature vs damage index for damaged pipe elbow mounted with EPDM rubber gaskets. Trial 2 of 2 indicates correlation is repeatable between days of operation.

It is likely that the trend seen in the above figures is due to the EPDM rubber gaskets, which change significantly in mechanical properties with temperature [37]. This boundary condition change can be interpreted as a change in the lumped k_1 and k_2 values in the two degree of freedom model developed in Section 3.1 .

A similar study was conducted on the second pipe elbow to investigate the effects of pressure on damage index with the EPDM gaskets installed. The test bed was operated up to 80°C

and pressurized to a maximum operating pressure of 8 psi. Operating data were collected on the test bed from the accelerometers and used to calculate damage index as before. In this experiment, between each trial of data collection, 0.5 psi of pressure was relieved from the tank with a manual valve. A 30-psi manual pressure gauge was used to measure the tank pressure for each trial. This resulted in the following damage indices

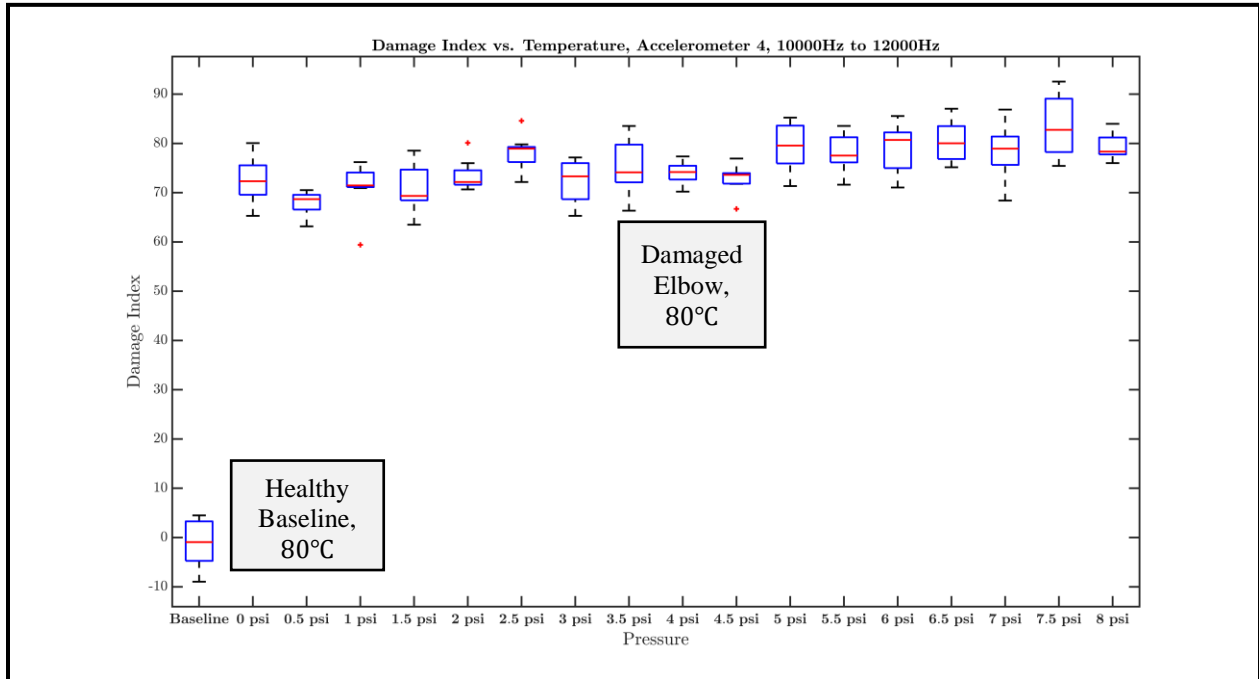


Figure 3-35: Pressure vs damage index for damaged pipe elbow with comparison to healthy baseline pipe elbow at 5 psi and 80°C

These data indicate that although a small positive correlation between pressure and damage index was seen, the mass removed from the elbow was still detected by the relative transmissibility method discussed for all pressures tested. The results presented in Figure 3-35 also strengthen the findings presented in Figure 3-33 and Figure 3-34 by showing that the variability introduced between 5 psi and 0 psi of operating pressure would not significantly bias the temperature vs damage index relationship. Figure 3-36 Shows an expanded view of Figure 3-35 without the baseline data.

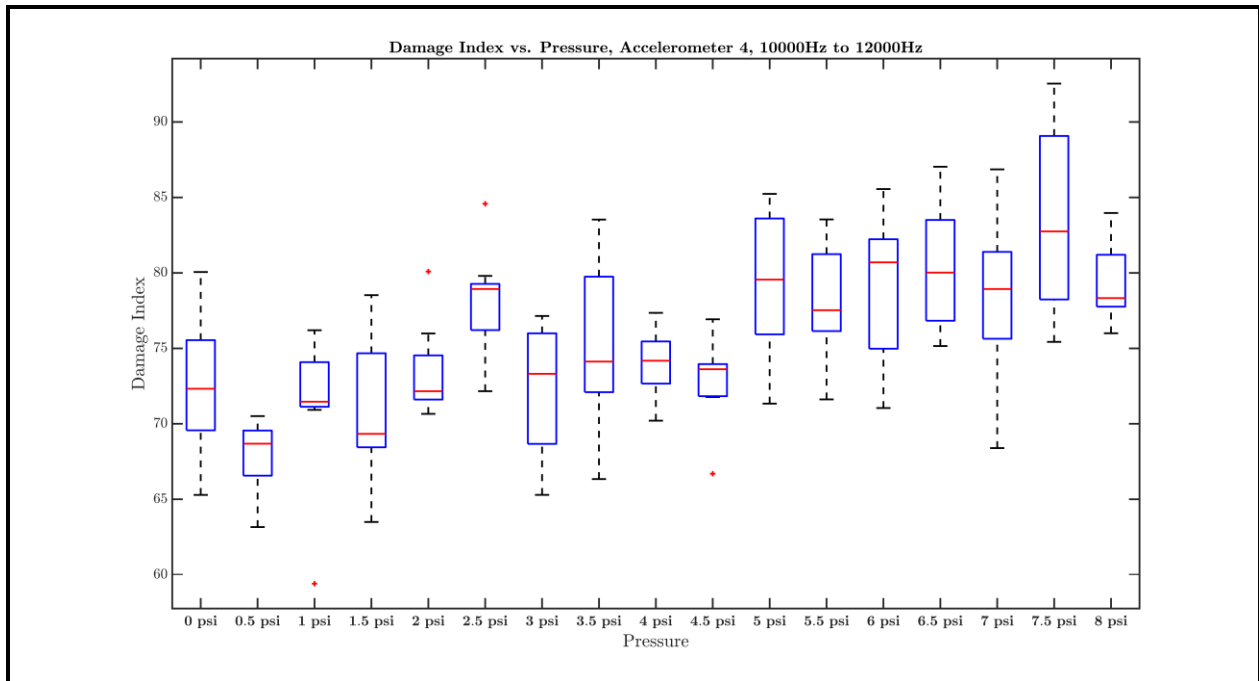


Figure 3-36: Damage index vs pressure on elbow mounted with EPDM rubber gasket shows positive correlation between pressure and damage index

It was noted that higher pressures corresponded to higher damage indices (in general) for the second pipe with 1.5% mass removed. One potential implication of this result is that higher operating pressures can enable increased sensitivity to change in mass. This could be caused, for example, by slightly increased compression on the rubber gaskets and subsequent stiffening of the boundary condition of the elbow mount.

This study would offer more insight if higher pressures were tested. Because a nuclear power plant typically operates at higher temperatures and pressures than were achieved in the operating test bed, it would be valuable to see how higher operating pressures affect the damage index measurement.

To further investigate the hypothesis that the correlation between pressure and damage index was caused by gasket compression due to operating pressure, a stiffer gasket material was used on the second pipe elbow with 1.50% mass removed. The temperature and pressure tests were repeated with Aramid/Buna-n gaskets. Figure 3-37 and Figure 3-38 summarize the temperature and pressure relationships found. Note that the absolute value of the damage index was not of

interest because the boundary condition changed significantly from the baseline conditions with EPDM rubber gaskets. The trend in damage index was the focus of this study.

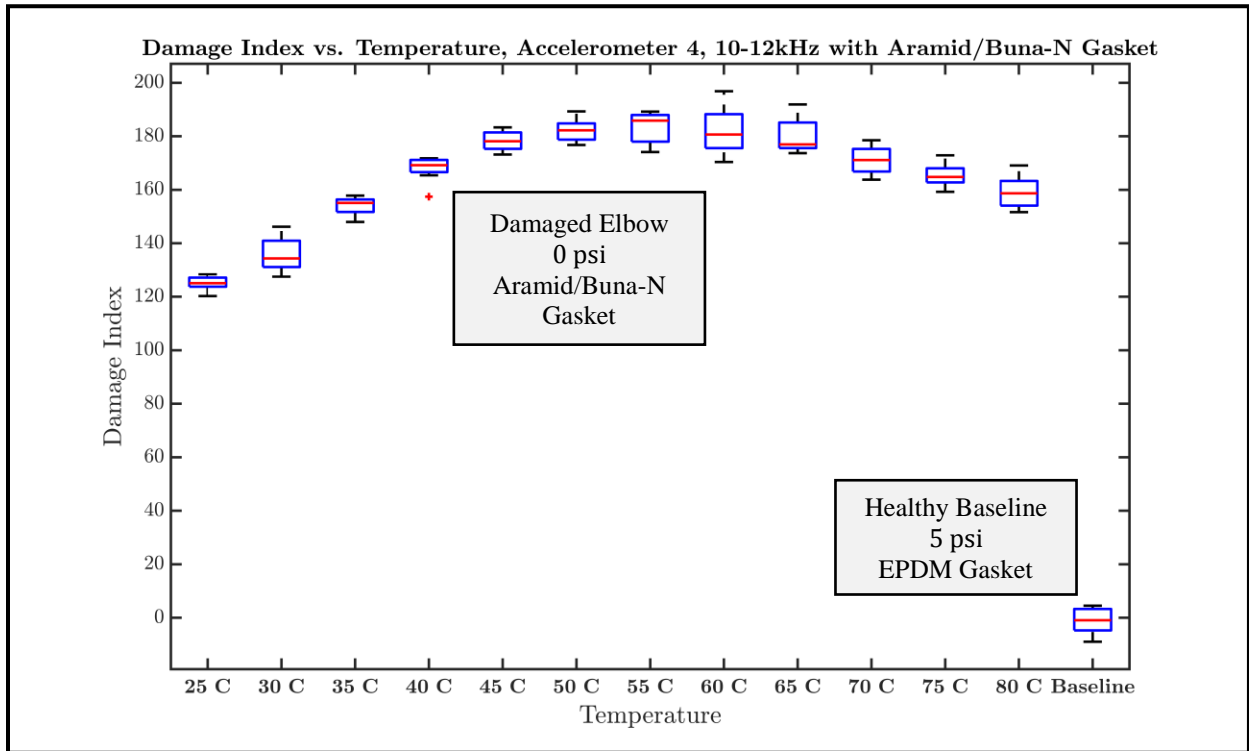


Figure 3-37: Temperature vs damage index for the second elbow with 1.50% mass removed, using Aramid/Buna n gasket material

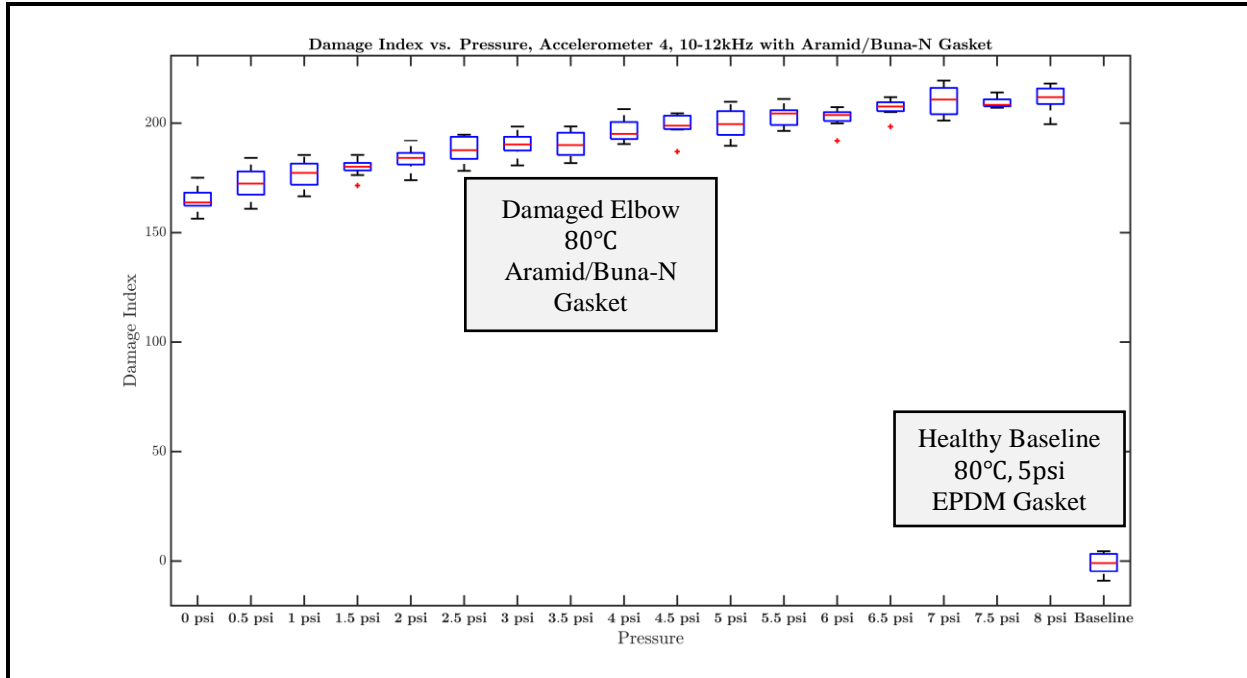


Figure 3-38: Pressure vs damage index plot for second elbow with 1.50% mass removed using Aramid/Buna-N gasket material, indicating similar trend between pressure and damage index.

These data showed a stronger relationship between pressure and damage index for the stiffer gasket material, and a different relationship between temperature and damage index. This result strengthens the hypothesis that the gasket was a significant factor in determining the temperature-damage index relationship. The pressure vs damage index result indicates that a similar relationship is maintained with different gasket materials. This could be interpreted to mean that the gasket is not the primary causal factor in the relationship between pressure and damage index, but that the gasket stiffness plays a role in determining the strength of this relationship, with softer gasket material corresponding to a weaker pressure vs damage index correlation. In this study, it was also observed that a stiffer gasket resulted in a clearer trend between damage index and pressure.

3.9 Conclusions and Next Steps

Local transmissibility function estimation was shown in this chapter to have the potential to be used as an indicator of distributed non-axisymmetric mass reduction on the inside of a pipe elbow. The given damage indices were shown to be less sensitive to daily variability in operating condition than to controlled reduction in pipe elbow mass. The model used to develop the data analysis approach for the experimental data consisted of a simple two degree of freedom oscillator, with the transmissibility between degrees of freedom becoming coupled as a change in mass on the inner diameter of the pipe cross section was factored in.

Future work might include a further examination of the variability in damage indices between elbow components. Variability was shown between the data of two elbow joints, and a further study of which indicators are consistent between elbows would add value to this detection strategy. Isolating random variation from variation due to operating conditions would also make the damage index method for damage detection more robust. A sensitivity analysis of the different operating conditions, both those covered herein – and additional factors like pressure drop across the elbow, flowrate, and water chemistry referred to in Equation 3-24 – would enable progress towards this end.

Additionally, a more sophisticated model of pipe vibration would enable a more targeted application of transmissibility analysis than the application demonstrated. Extensive work on modeling transient pipe vibrations with the transfer matrix method has been done in [38]–[40] which would allow for transient modeling of pipe element vibration in the context of a wider pipe network. The key challenge in applying this work to modeling the piping in the test bed used for this research was adequately reproducing an input signal from flow and pump input sources. A model for the pressure power spectrum was developed in [41], [42] that would approximate flow input spectra, and pump input spectra could be directly measured from the pump housing, but there existed no capabilities on this test bed to verify the model of flow/pump input with experimental data. Therefore, implementing and validating this model would have exceeded the scope of this thesis, which served instead as a proof-of-concept for the relative transmissibility analysis discussed and a characterization of sources of variability in the damage detection method. Note also that developing a clearer sense of the required frequency range and measurement resolution for this method would allow for sensor optimization and reduction of cost.

4. Early-Stage Corrosion Detection with Smart Film Technology

4.1 Background on Smart Film Technology

The smart film studied in this work refers to a polymeric monolayer grown on the surface of silicon wafer samples. In recent work by Jennings and Deng at Vanderbilt University [30], this smart film was shown to chelate, or bond with, iron ions out of solution. The film formed cross-links in the polymer matrix with these ions, resulting in a changed dynamic modulus corresponding directly to the level of chelation in the film.

The complex shear modulus is given by

$$G = R + jQ \quad (4-1)$$

where R is the shear storage modulus, Q is the shear loss modulus, and G is the complex shear modulus. In Deng's work, a fully chelated film was shown to have a 15% increase in mass, a 47% decrease in shear loss modulus Q, and a 65% increase in shear storage modulus R. These data were gathered on dry films, so dry films were used in this research as well.

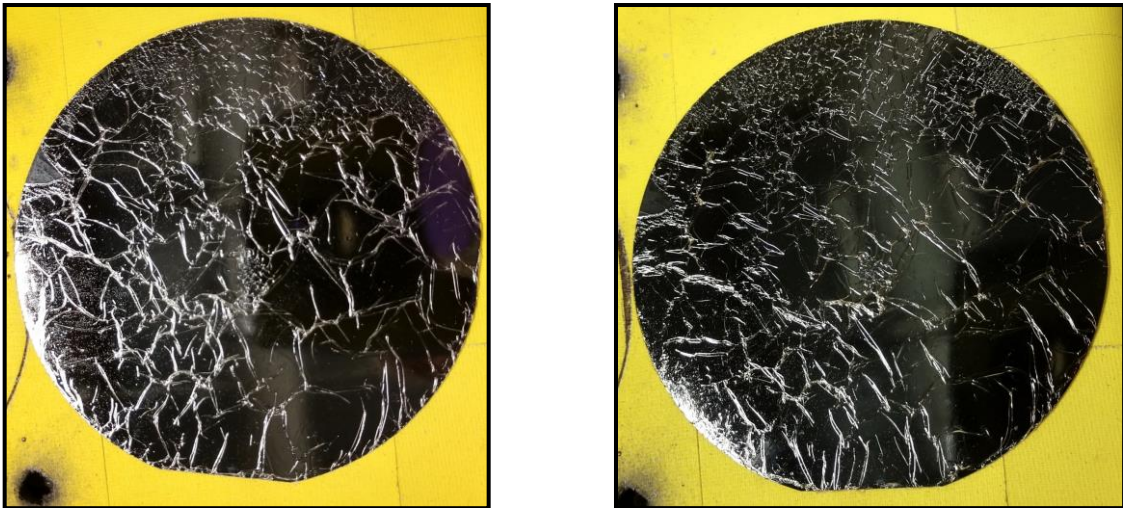


Figure 4-1: Silicon wafer before (left) and after (right) chelation. Visually, only a slight yellow coloration in the chelated film distinguishes their appearance

Deng's result suggested that the smart film would become less viscous as it cross-linked with iron ions out of solution because of its modulating complex modulus. Therefore, an increase in damping could be expected with the addition of the film to a bare surface due to constrained layer damping effects, and a subsequent decrease in modal damping could be expected with the chelation of the smart film. Additionally, because the distributed mass increases with both film deposition and chelation, the frequency response function peaks could also be expected to shift left between each stage if the wafer-film system was sufficiently sensitive to changes in film mass and damping.

Analytical determination of the relationship between complex modulus of a thin film and the overall response of a wafer-film system was beyond the scope of this work. Here, experimental results are used to evaluate the sensitivity of a film-substrate system to the chelation mechanism demonstrated by [30]. Determining how robustly the film's absorption of iron ions would be detectable by vibroacoustic methods was the key point of interest in the following experiments. Insights both from experimental data and finite-element modelling of the wafer-sensor system are developed.

4.2 Effects of Chelation on Vibroacoustic Behavior of Silicon Wafers

In this study, the dynamic properties of silicon wafers were evaluated before smart film deposition, after smart film deposition, and after chelation of the smart film layer. The goal of this study is to evaluate the observed mechanical property shifts seen in the smart films in [30]. This trial was conducted on silicon wafer samples because their stable surface chemistry and smooth surface finish enabled consistent film growth.

4.2.1 - Test Setup and Design

A rigid fixed boundary condition was achieved using a bolted fixture to secure the silicon wafers against the mounting plate on the outlet of a Selenium DD3300Ti DPD acoustic actuator. This design prevented flanking around the edge of the wafer and maximized energy transfer between the actuator and the wafer. It was assumed that the diameter of the steel mounting plate

hole corresponded to size of the unclamped plate used in the modeling of the wafer. Figure 4-2 illustrates the test fixture design.

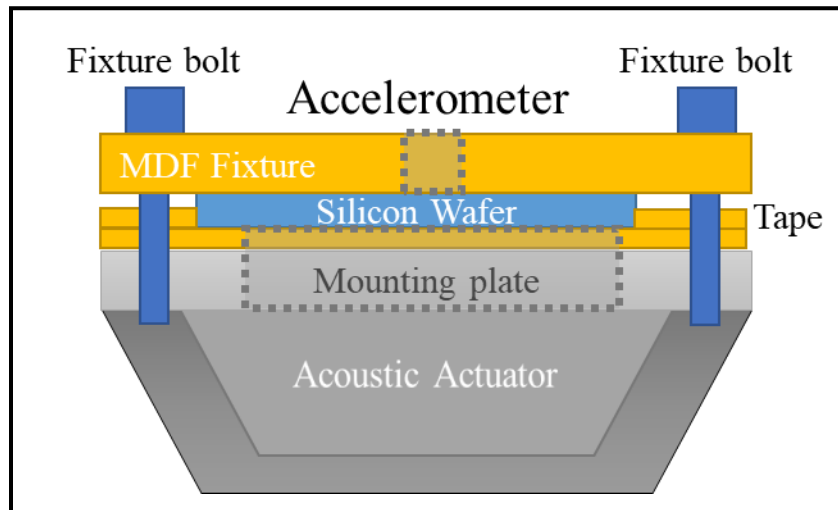


Figure 4-2: Side-view diagram of test fixture for Si wafer trials

The film deposition process at this phase of the project required clean wafer surfaces, achieved either through oxygen plasma etching or piranha cleaning. Both of these processes would have damaged the single-axis accelerometer used to collect data, so the accelerometer was removed between stages of the test. Ten measurements were taken at each stage of film growth and chelation in order to account for variability between accelerometer placements. Between each measurement, the accelerometer was removed and re-adhered to the wafer. Two wafers were tested to capture variability between wafers and film depositions.

Loctite 454 superglue was used to adhere the accelerometer to the center of the sample. The center of the wafer was marked using a cylinder center-finder tool. A Milwaukee M12 Fuel Hex Driver was used with a constant clutch setting of 4 to install the fixture fasteners with consistent torque between trials. A 3-inch circle of additional gaffer's tape was marked for aligning the flat edges of the wafers to achieve consistent alignment of the wafers between trials.

Gaffer's tape was used on the steel mounting bracket to prevent stress concentrations on the silicon wafer surface. Earlier trials revealed that the silicon-steel interface caused fractures in the more brittle silicon wafer. To prevent this, the tape was used to reduce stress concentrations on

the silicon wafers and ensure sample survivability between trials without significantly compromising the fixed boundary condition of the test setup. The test fixture is shown in Figure 4-3.

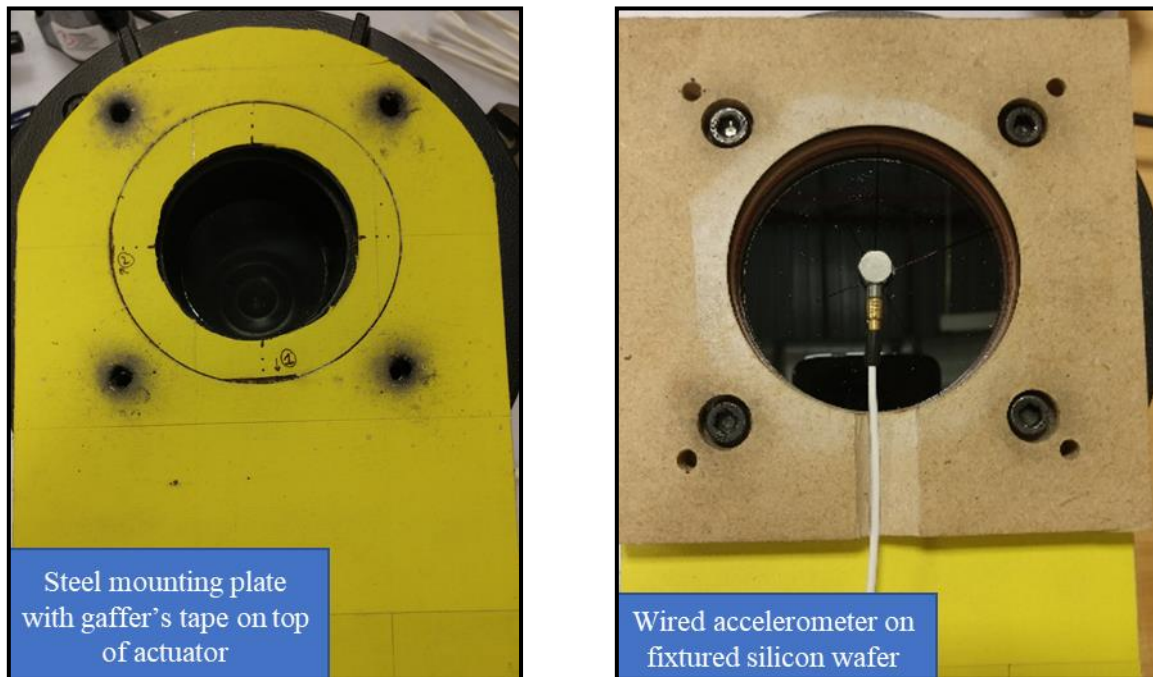


Figure 4-3: Test fixture (left) with Si wafer installed (right)

An Agilent 33250A function generator was used to generate a linear input sweep from 100 Hz to 25.6 kHz at 100 mVpp over a 50 ms time span. The input signal was amplified by approximately 22dB by a QSC Audio RMX 2450 Professional Power Amplifier before driving the acoustic actuator. This amplified signal was routed to an NI 9234 DAQ card and used as the input time history for the frequency response function estimation. The measured response of the PCB C65 100 mV/g single-axis accelerometer was used as the response for frequency response function estimation.

4.2.2 - Silicon Wafer Test Results and Discussion

The first silicon wafer was evaluated for baseline frequency response function without a film addition. The ten frequency response function estimations of the wafer are reported in Figure

4-4. Note that the small peak to the left of the first labeled peak had a coherence measurement consistently below 0.8, so it was ignored. The first three peaks had coherence values of 0.95 or above.

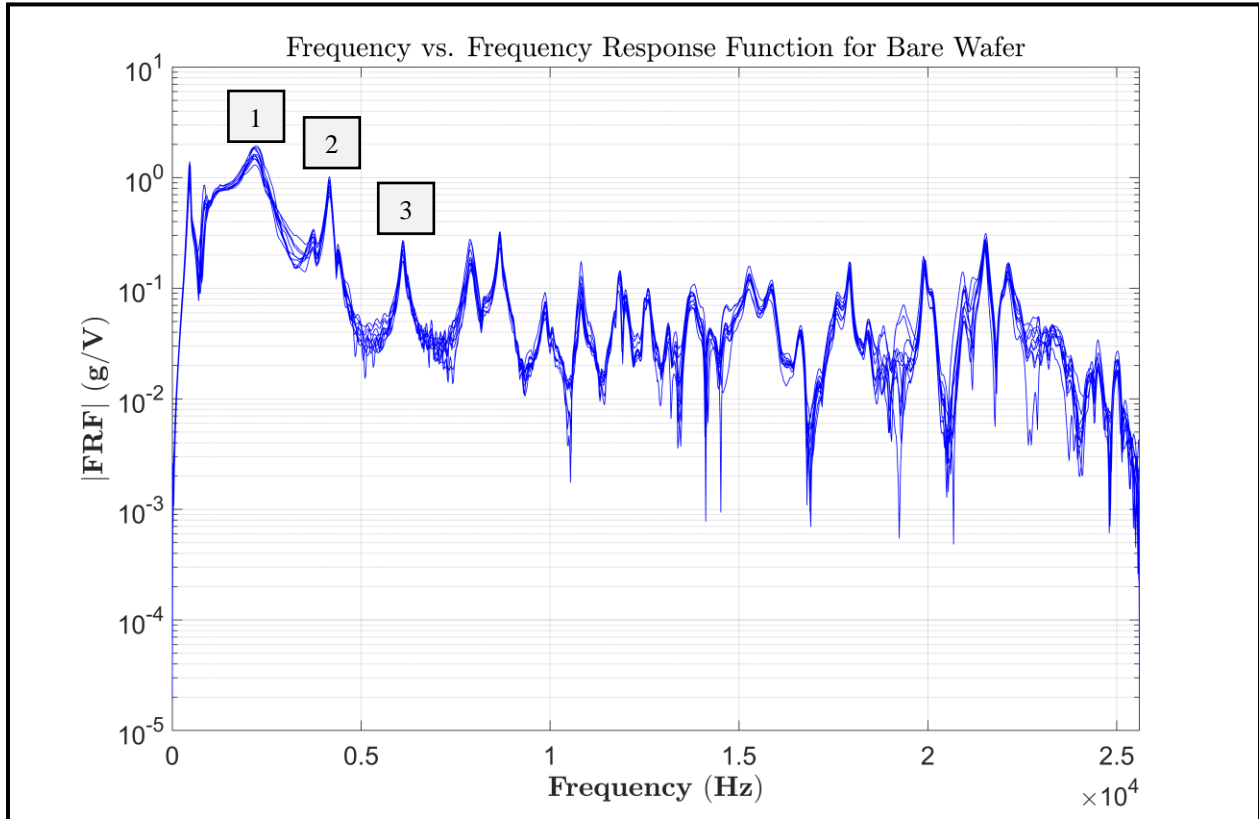


Figure 4-4: Frequency vs frequency response function for bare wafer, with first three peaks labeled

Qualitatively, the addition of film to the silicon wafer was expected to increase damping and lower resonant frequencies, which would appear in the FRF as rounded peaks compared to the baseline wafer with no film. This is because in addition to the damping effects of the interface between wafer and film, the mass of the film was expected to lower the resonant frequencies of the wafer.

With film chelation, the resonant frequencies were expected to further reduce with the 15% increase in mass of the film. The resonant peaks were also expected to sharpen with the decrease in viscous behavior of the film.

These results would only have manifested significantly in the frequency response functions if the overall system was sensitive enough to the changing complex shear modulus and mass of the film. All measured frequency response functions for wafer 1 are reported in Figure 4-5.

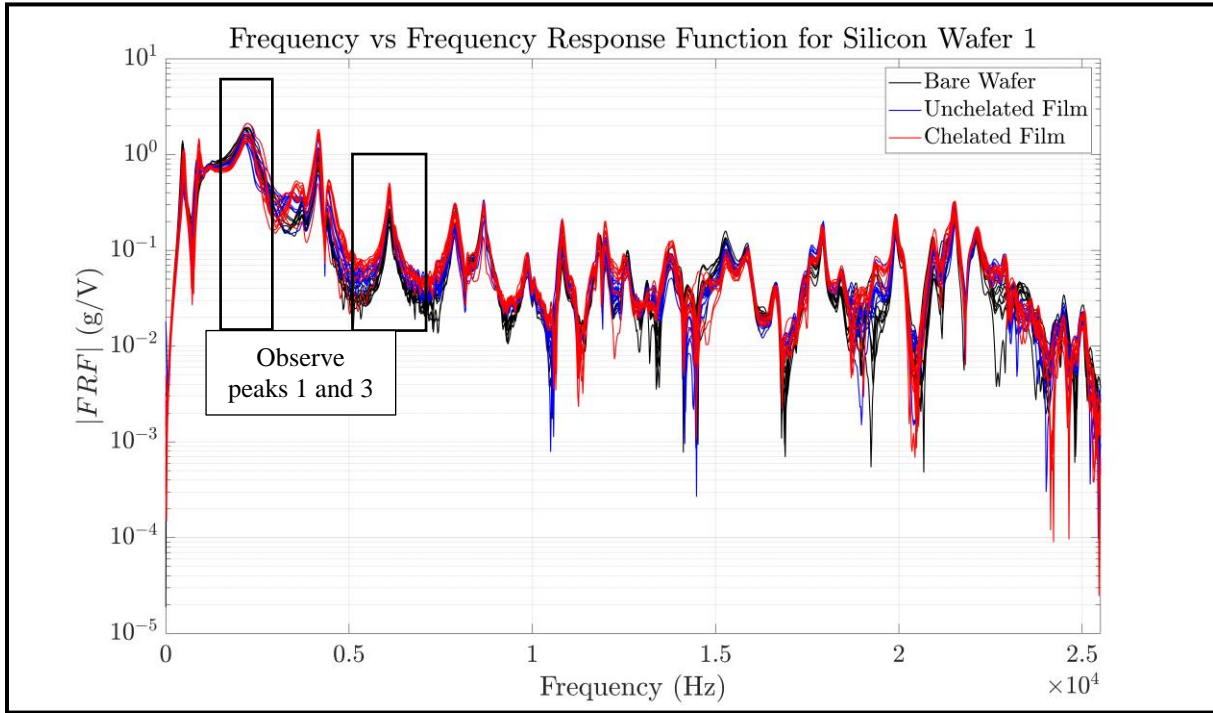


Figure 4-5: Frequency vs frequency response function for wafer 1, with 2200 Hz and 6100 Hz peak highlighted for further investigation.

Figure 4-5 indicated that the frequency response function magnitude was generally increased across the board with the addition of the film and the chelation of the film. The presence of chelated iron ions in the film was confirmed with IR spectroscopy, but the exact degree to which chelation occurred was not measured for the films. It was noted, however, that the film had additional un-filled capacity for chelation at the time of testing. The frequency response functions in Figure 4-5 do not show the expected trends associated with significant damping and mass changes. However, peak frequencies were of interest because their magnitudes appeared sensitive to the addition and modulation of the film.

Framing the frequency response function to show the peak at approximately 6100 Hz showed the peak amplitude trend illustrated in Figure 4-6.

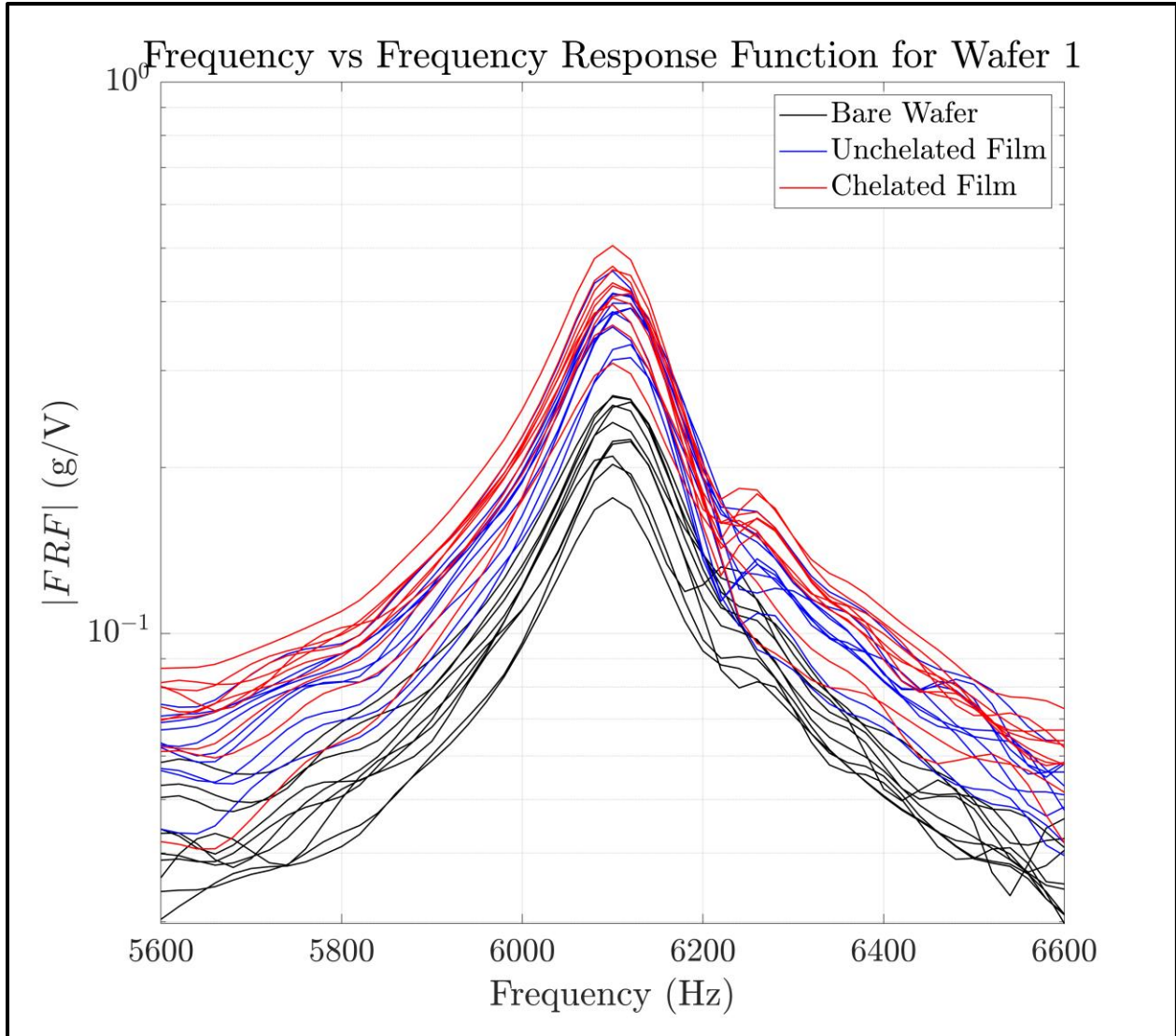


Figure 4-6: Frequency response function for wafer 1 between 5600 Hz and 6600 Hz, illustrating a trend between stage of film and peak amplitude.

Integration of the measured frequency response functions with respect to frequency was performed to calculate damage indices relating to each trial. For each frequency response function $H(\omega)$, the frequency bounds $f_1 = 5600 \text{ Hz}$ and $f_2 = 6600 \text{ Hz}$ were chosen. This integration was approximated with the summation function in MATLAB across the specified frequency bounds.

$$DI = \int_{f_1}^{f_2} |H(\omega)| \quad (4-2)$$

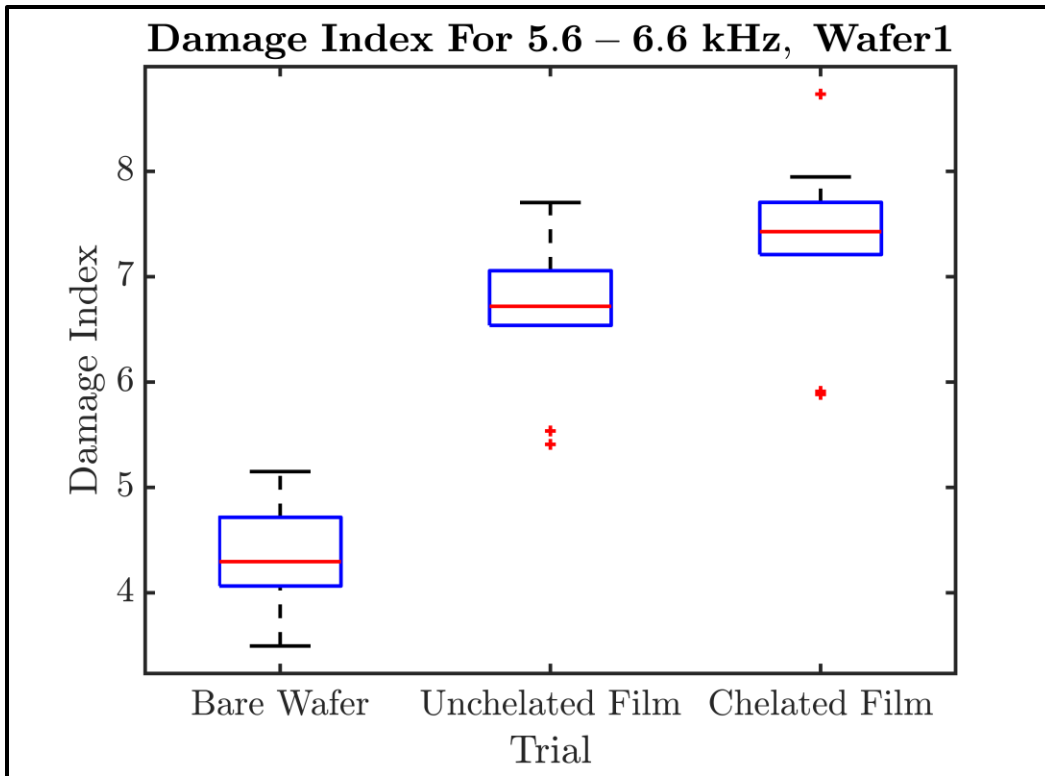


Figure 4-7: Damage indices for each stage of chelation in wafer 1, from 5.6-6.6 kHz, show a positive relationship between chelation and damage index.

This result suggested that both the addition of the film and the chelation of iron ions increased the resonant response of the wafer system at the 6100 Hz peak. The same test was repeated for a second wafer. Bare wafer data were not collected in this trial due to time constraints. The 6100 Hz peak is plotted in Figure 4-8.

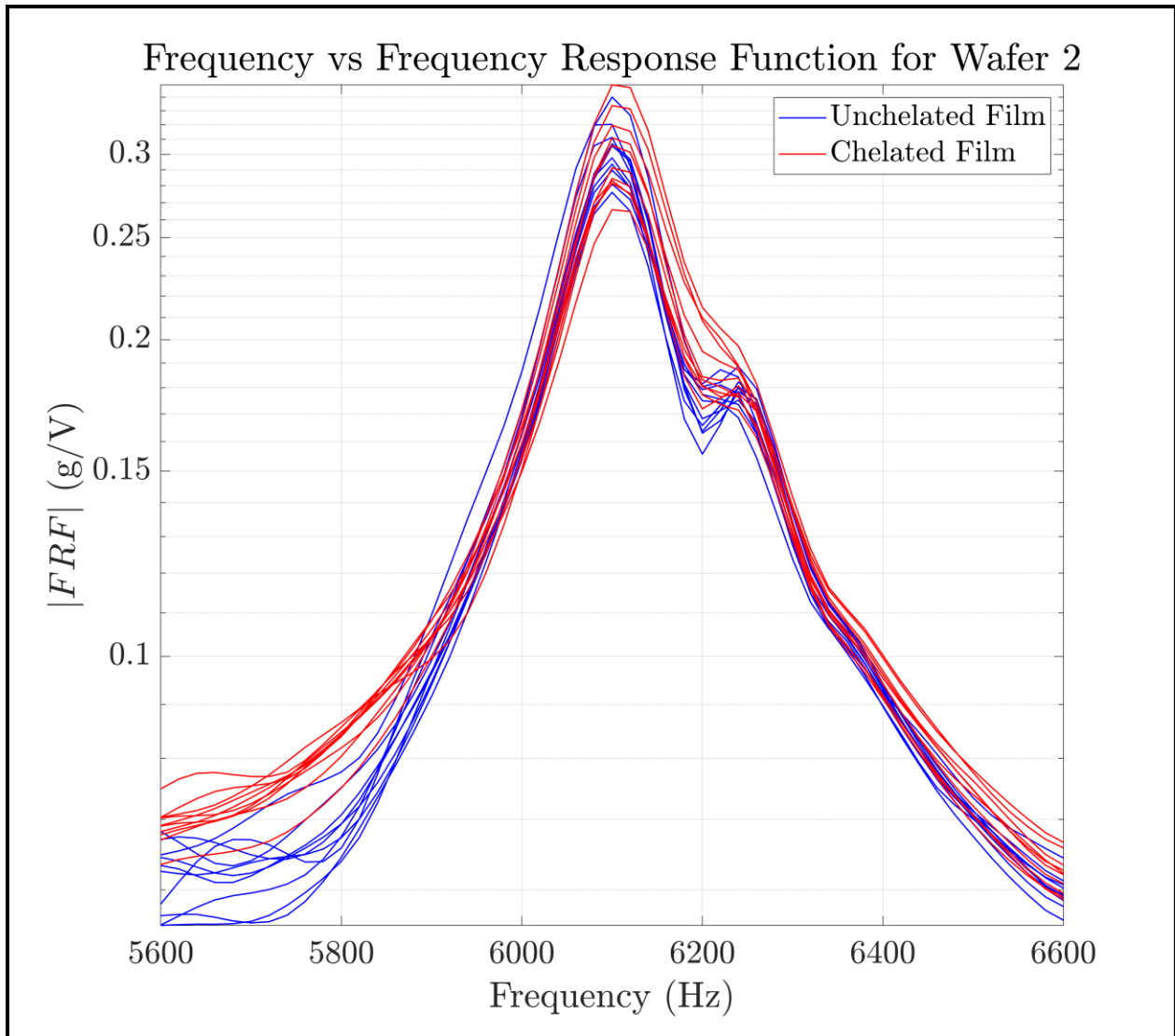


Figure 4-8: Frequency response function peak at 6100 Hz for wafer 2

Figure 4-8 indicates a similar trend between peak amplitude and the introduction of chelation into the smart film. The damage indices were re-plotted with data from wafer 2 and are reported in Figure 4-9.

It is difficult to establish a relationship between chelation of the film and the peak amplitude changes observed without quantitative data on the degree to which the film was chelated. However, for two wafers each independently instrumented ten times per stage of film growth/chelation, an increase in resonant peak amplitudes was observed from the non-chelated film to the chelated film.

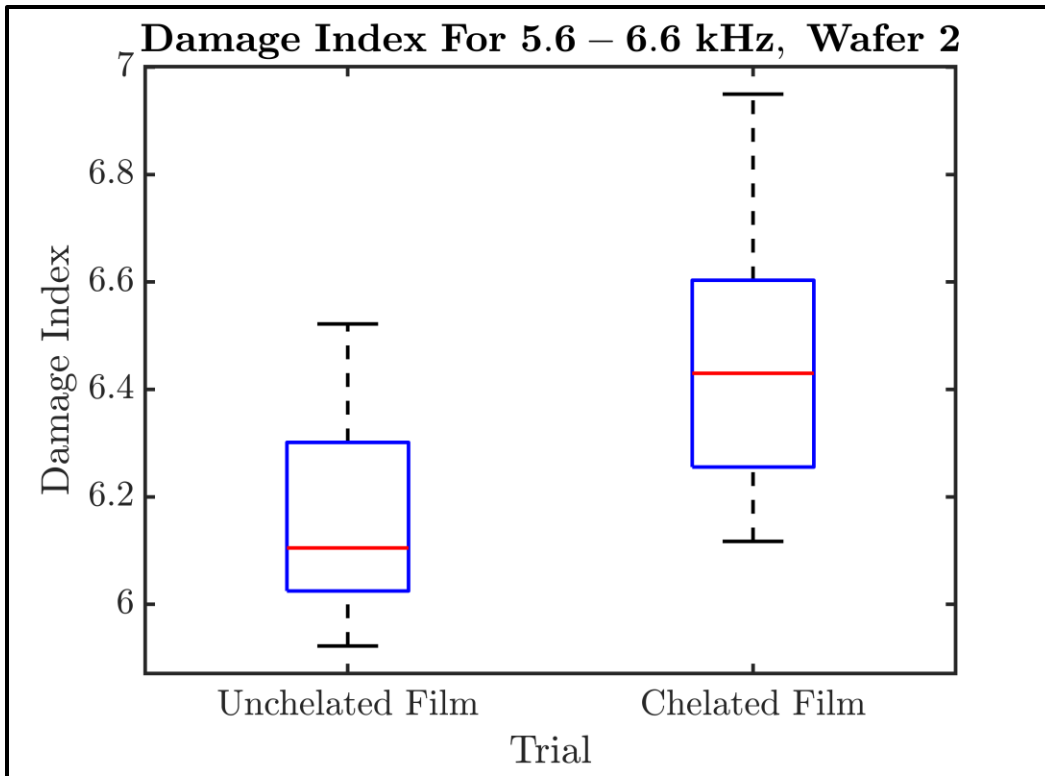


Figure 4-9: Damage indices for each stage of chelation on the second wafer.

Peak shifting was also observed at the first frequency response function peak. This observation showed that for both wafers tested, the first peak was sensitive to the addition of the film and its chelation. Figure 4-10 shows a plot of the frequency response function near this peak.

A similar damage index calculation was made between 1000 Hz and 3500 Hz for the first peak of each wafer's frequency response function. These results are shown in Figure 4-11.

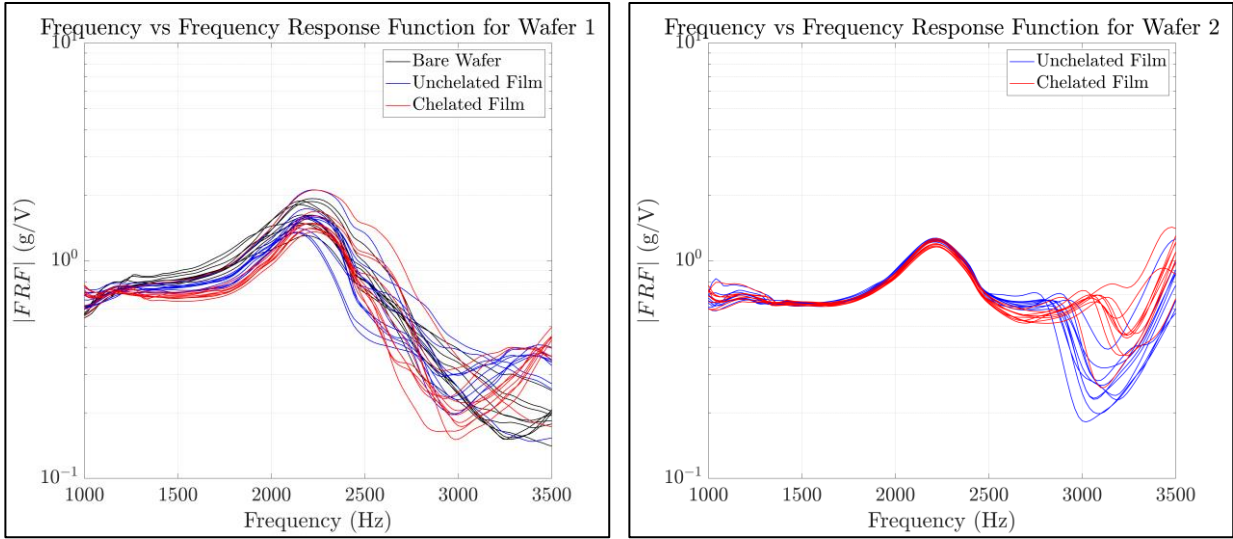


Figure 4-10: First frequency response function peak for wafer 1 (left) and wafer 2 (right) show peak frequency increase with chelation of the film.

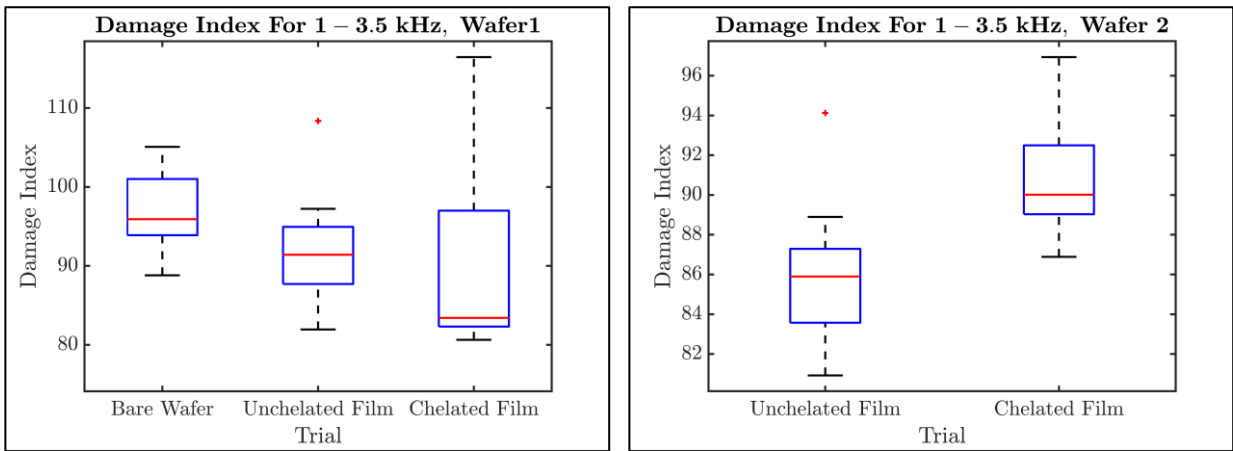


Figure 4-11: Boxplots of damage indices calculated from 1 kHz to 3.5 kHz for wafers 1 and 2 indicate opposite trends in damage index for each wafer. Note that axes are not scaled equally.

The peak shifting and peak intensity changes observed in the first and third frequency response function peaks were unique to the data, because many other frequency response function features did not show reproducible changes in frequency response with chelation between wafers.

The question of why peaks one and three were sensitive to chelation in the film, and why they behaved in the way they did, was addressed with a modeling effort to understand the mode shapes governing the frequency response function of the silicon wafer.

4.2.3 - Silicon wafer model development for interpretation of experimental data

The bare silicon wafer was first analytically modeled as an isotropic [43], rigidly mounted circular plate. The analytical model developed in [44] was used with clamped boundary conditions to generate modal frequencies and mode shapes.

The properties used to model the silicon wafer are given in Table 4-1. These properties were used for both the analytical and the numerical model. Note that the wafer is assumed isotropic with Young's modulus and Poisson's ratio based on [43].

Table 4-1: Model parameters of the bare silicon wafer and test setup used

Radius	a	26.59 mm
Thickness	h	381 μm
Area density	σ	.884 kg/m^2
Young's Modulus	E	130 GPa
Poisson's Ratio	ν	0.28

$$I_n(\lambda_{nm}a)J_{n+1}(\lambda_{nm}a) + J_n(\lambda_{nm}a)I_{n+1}(\lambda_{nm}a) = 0 \quad (4-3)$$

In the frequency equation shown in Equation 4-3, J_n and I_n are the Bessel functions and modified Bessel functions of order n , respectively. a is the unclamped radius of the plate, and $\lambda_{nm}a$ is the unknown root of the frequency equation for mode nm . The natural frequency (in radians per second) of mode nm is determined with

$$p_{mn} = \lambda_{nm}^2 a^{-2} \sqrt{D/\sigma} \quad (4-4)$$

The displacement of the wafer for a selected mode is given in polar coordinates by:

$$w(\varrho_{nm}, \theta) = R(\varrho_{nm}) * \begin{bmatrix} \cos(n\theta) \\ \sin(n\theta) \end{bmatrix} \quad (4-5)$$

In the displacement equation shown, θ is the angular position on the surface of the plate, r is the radial displacement along the wafer, and $\varrho_{nm} = \lambda_{nm}r$.

$$R(\varrho_{nm}) = \frac{1}{I_n(\lambda_{nm}a)} [J_n(\varrho_{nm})I_n(\lambda_{nm}a) - J_n(\lambda_{nm}a)I_n(\varrho_{nm})] \quad (4-6)$$

This analytical model was used to calculate natural frequencies and mode shapes of the circular plate. Note that n corresponds to the number of nodal diameters and m corresponds the number of nodal circles for each mode. The calculated natural frequencies from the analytical model are reported in Table 4-2.

Table 4-2: Tabulated natural frequencies from analytical model (Hz)

n	m			
	1	2	3	4
0	1973	7680	17208	30551
1	4105	11748	23192	38442
2	6735	16333	29707	46876
3	9854	21440	36755	55850
4	13453	27057	44324	65354

To account for the effects of mass-loading from the transducer and the effects of the smart film addition to the wafer system, a numerical model of the wafer was developed.

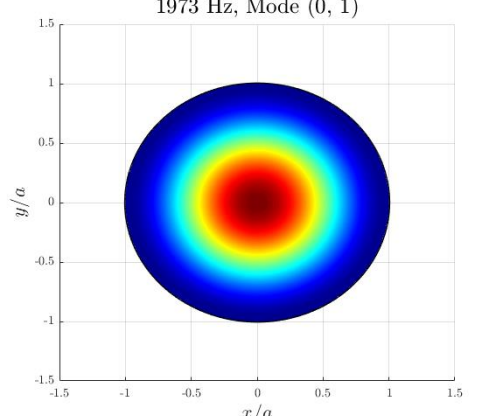
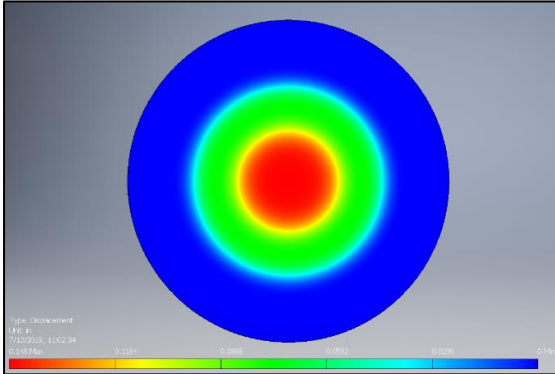
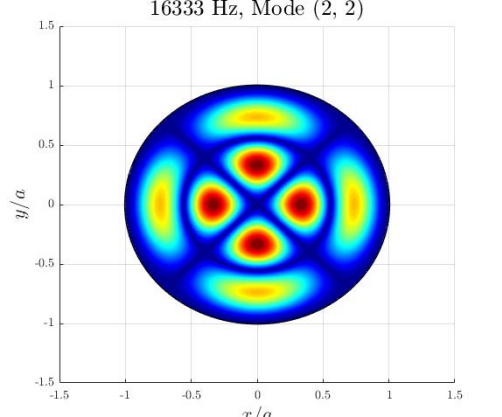
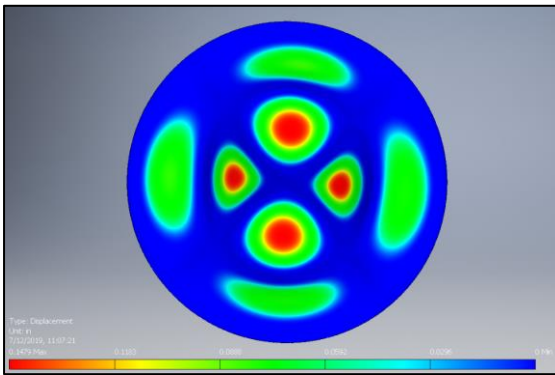
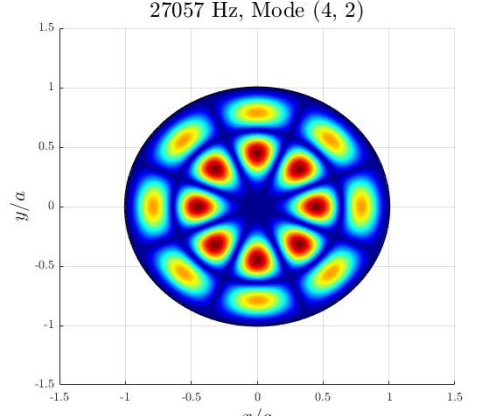
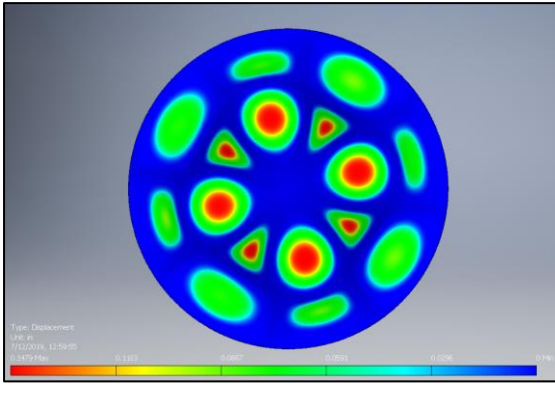
Table 4-3: Tabulated natural frequencies from numerical model (Hz)

n	m			
	1	2	3	4
0	1970	7659	17128	30328
1	4098	11708	23051	38173
2	6719	16267	29492	46399
3	9825	21326	36451	–
4	13402	26886	43979	–

Table 4-4: Error between analytical and numerical models of silicon wafer

N	m			
	1	2	3	4
0	0.14%	0.28%	0.46%	0.73%
1	0.16%	0.34%	0.61%	0.69%
2	0.23%	0.41%	0.72%	1.02%
3	0.29%	0.53%	0.83%	–
4	0.38%	0.63%	0.45%	–

Table 4-5: Comparison of selected analytical and numerical mode shapes for bare silicon wafer

Mode	Analytical Model	Numerical Model
(0,1)	<p>1973 Hz, Mode (0, 1)</p> 	
(2,2)	<p>16333 Hz, Mode (2, 2)</p> 	
(4,2)	<p>27057 Hz, Mode (4, 2)</p> 	

The numerical model was compared to the bare-wafer analytical model results to verify the accuracy of the numerical model. Modal analysis of a fixed wafer was performed in Autodesk Inventor Professional 2019. The numerical scheme of this software is based on the finite element method. The first 50 modes were calculated in the numerical modal analysis study. Natural frequencies within the first four nodal diameter and circle groups of the numerical model are reported in Table 4-3. The percent error between analytical and numerical results is reported in Table 4-4. A comparison of selected analytical and numerical mode shapes is summarized in Table 4-5. Note in Table 4-5 that the blue color corresponds to zero displacement, and the red corresponds to maximum displacement.

The results of this comparison indicated that, excepting the highest-frequency mode studied, the finite-element model of the wafer reported natural frequencies within one percent of the expected analytical closed-form solution. It also indicated that the finite element model reproduced the expected mode shapes with reasonable fidelity within the 0 – 25.6 kHz frequency range.

This numerical model was then used to account for experimental factors beyond the scope of the analytical model. Because the sensor used was 2.8 g and the mass of the unclamped portion of the silicon wafer was approximately 2.0 g, The finite-element model was adjusted to include the mass-loading of the accelerometer in the system as a mass rigidly bonded to the center of the wafer.

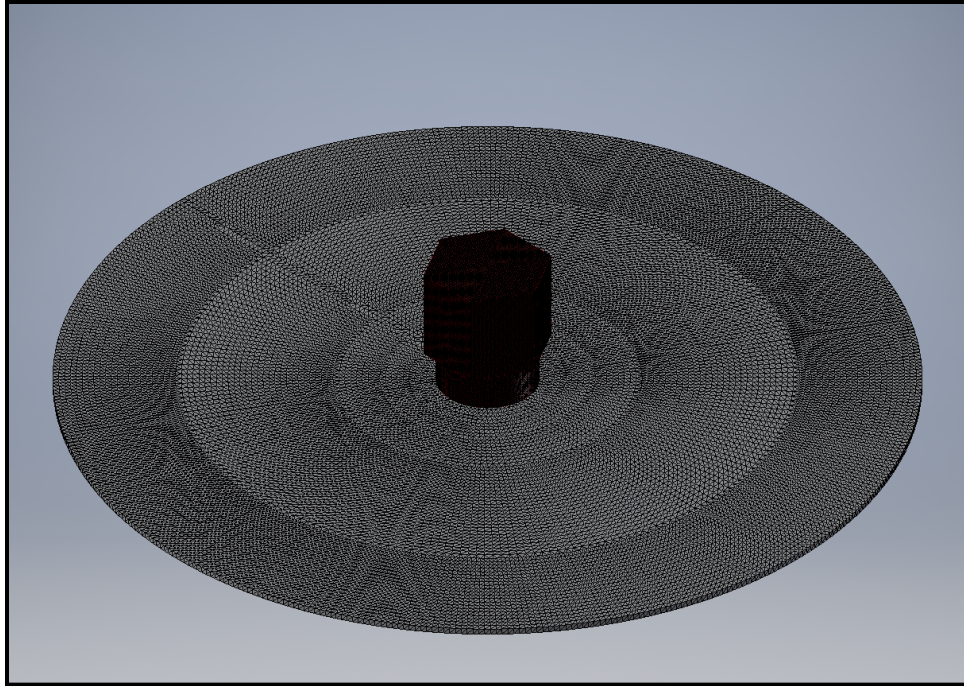


Figure 4-12: 3-dimensional rendering of wafer modeled with added mass of accelerometer; mesh shown

A similar modal analysis was performed on the updated wafer-mass system. This study produced the first four mode shapes as shown in Figure 4-13.

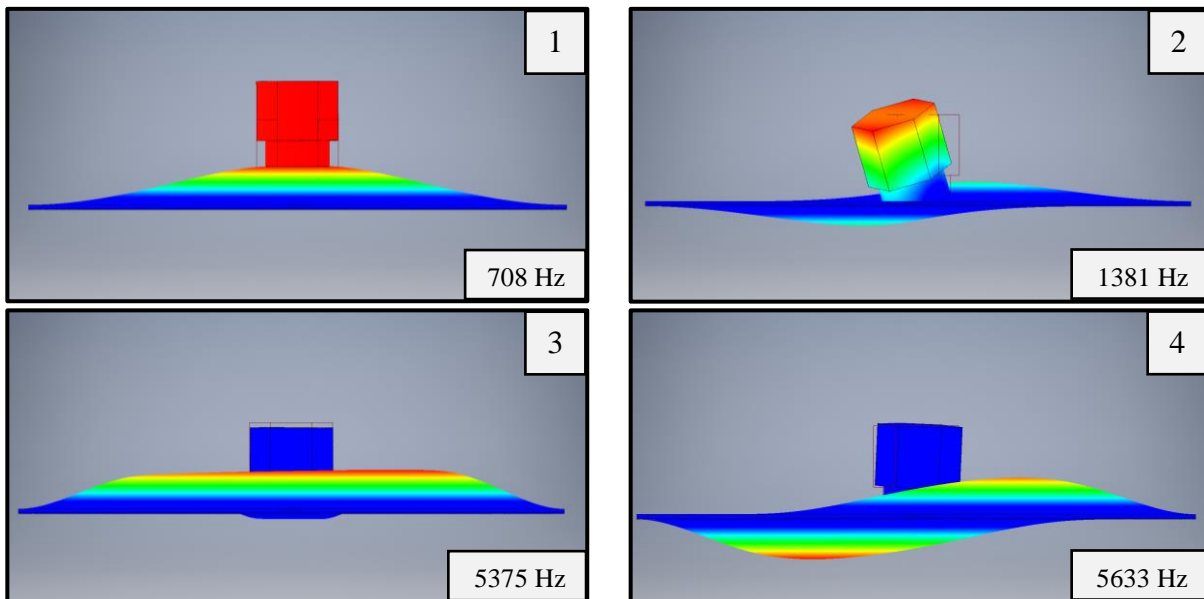


Figure 4-13: First four numerically modeled mode shapes of silicon wafer with added accelerometer mass

This numerical model suggested that the single-axis accelerometer used in the experiment would move vertically only in the first and third modes of vibration of the plate-accelerometer system. This finding indicates that although changes in dynamics due to the film may affect other modes of vibration, the instrument used in this study would be most likely to detect changes in these modes.

Regarding why the third mode saw better repeatability than the first mode, it was hypothesized that the frequency of the first mode was too low to be sensitive to the modulating properties of the smart film. In the model, the difference between first and third mode frequencies was almost an order of magnitude. In the experimental data, the first and third modes (as interpreted and selected) were roughly 3900 Hz apart (2.2 kHz to 6.1 kHz). The higher frequency of the third mode may have made it more sensitive to changing complex shear modulus and mass of the smart film.

Because of the design of the experiment and equipment limitations, it is difficult to draw strong conclusions about the detectability of smart films in their current state of development. There were indications of trends between film chelation and frequency response function properties of the silicon wafer-film systems, but these trends were not completely reproducible between silicon wafers. Modeling gave some suggestions about the mechanisms at play in the system, but a clear understanding was not reached. Additionally, the method used to characterize degree of chelation in the film is neither quantitatively precise nor safe to use on samples intended for re-use, as the silicon wafer must be cut in order for the IR spectroscopy measurement to be made. Studies on the relationship between film chelation and vibroacoustic properties, therefore, need a different way of quantifying chelation in order to develop strong correlations between degree of chelation and vibroacoustic indicators (peak frequency, damage index, etc.).

Because the mass-loading of the accelerometer was significant in this trial, if a laser vibrometer were used instead of a bonded accelerometer, this would allow for a more controlled set of data on either a silicon wafer or some other small sample substrate on which the smart film would be grown. Laser vibrometry offers the advantage of making no contact with the vibrating sample while enabling high-precision and high-frequency measurements to be made on the surface of the sample. This modification to the test design would likely yield stronger insights into the

effects of the smart film on substrate properties because it would also eliminate the variability associated with repeatedly adhering the accelerometer to the silicon wafer surface.

With the research presented above, it can be concluded that some experimentally measured changes in silicon wafer frequency response functions were reproducible between wafers and between independent adhesions of the accelerometer to the wafer surface. This change manifested itself most consistently as an increase in peak magnitude at the third peak of the experimental frequency response function. Refined experimental design as discussed above would allow the relationship between degree of chelation and vibroacoustic properties to be more thoroughly understood and evaluated for their potential in nuclear power plant applications.

4.3 Implications of Smart Film Technology on the Nuclear Industry

Directly detecting local corrosion rates in real-time on the inside of an operating section of pipe is a non-trivial technical challenge. However, if this goal can be achieved, it would significantly improve operator insights into the nature of the mechanisms by which corrosion occurs. Improving temporal and spatial resolution of knowledge about the early onset of corrosion will be an important step in minimizing corrosion-related failure in nuclear power plant pipes.

The coupling between smart film chelation and vibroacoustic response measurements is one way to approach this challenge. By directly relating the degree of cross-linking to a normalized damage index with respect to a ‘healthy’ baseline, the rate of corrosion can be inferred. This film must maintain stability over long periods of time under high-temperature and high-pressure operation. It must also be successfully applied on the inside of a pipe and be detectable from the outside by vibroacoustic or some other methods. If these requirements can be met, then the potential for disruption in the nuclear industry is clear.

In this study, a preliminary experimental sensitivity analysis of a relatively stiff substrate (i.e. silicon wafer) indicated that vibroacoustic methods were shown to reveal some change in response after both the addition and chelation of smart films. Because the film technology was nascent at the time of this research, tests on metallic substrates or with a quantifiable degree of chelation in the film were not possible. However, it was concluded that with the addition of some degree of chelation in the film, resonant peaks were shown to increase in their response magnitude,

indicating increased transmissibility between the voltage source and the accelerometer. Assuming that the acoustic actuator and accelerometer remained unchanged throughout the study, this implies that the transmissibility between the acoustic actuator and the opposite side of the wafer was also increased after film chelation.

5. Summary and Conclusions

The work conducted herein serves as a proof of concept for real-time vibroacoustic degradation state monitoring techniques and technologies. The use of transmissibility between degrees of freedom with guidance from a relatively simple model of a pipe cross section was shown to provide meaningful information on the degree of mass transfer in a pipe elbow. Sources of variability – temperature, pressure, fitting installation, day-to-day operation variation, and gasket stiffness – were interrogated for their effects on relative transmissibility damage index estimation. The effect of smart film technology on a silicon wafer substrate was also characterized with frequency response function estimation. The results of this experiment showed the need for more refined testing methods to robustly interrogate the film in its current scale, but the experiment also showed potential with the third mode of vibration of the silicon wafer-accelerometer system, which consistently exhibited increased frequency response function peak magnitude at its third mode of vibration with the addition and chelation of the smart film.

Potential next steps for the detection of late-stage corrosion in pipe networks include interrogation of different fittings (tees, different pipe thicknesses), model development to include transfer matrix methods and turbulent flow-driven input spectra, and further variability characterization of the operating test bed. For one, a similar study to this could be conducted on a similarly representative pipe tee, and on pipe structures downstream of these fittings which have been shown to degrade as a result of downstream flow disruption caused by the fittings [29]. Although the challenge of adequately modelling vibroacoustic input from flow and pump proved itself to be beyond the scope of this work, more advanced modeling, perhaps including the work shown in [39], [40], might better capture the modal coupling phenomena explored herein. The exploration of coupling between axial and bending modes would also be of interest in this line of inquiry. Although the relationship between bending and torsional modes of vibration provided interesting results and was emphasized in this research, preliminary FEA models also show a significant number of modes in a simple pipe elbow which would best be described as some combination of bending and axial motion. It would also be useful to introduce more realistic corrosion-like damage into the pipe fittings than a uniform reduction of material.

Other sources of variability, such as flowrate, were not characterized in this research due to lack of instrumentation. However, developing a picture of flow-induced vibration and transmissibility would benefit from this measurement, as well as more detailed digital pressure measurements in proximity to the fittings of interest (in this research, only the tank pressure was measured with an analog sensor). Finally, a sensitivity analysis of the different ‘non-damage’ operating variables that can affect damage index measurement was initially conducted with temperature, pressure, and gasket material. The framework for analyzing these variables was laid out for future experimental development. Note again that the range of variability tested in these experiments was much wider than the expected range of a steady-state operating plant in which this technology would be used.

The relationship between smart films and the vibroacoustic properties of their substrates is also an area of potential discovery. The development of smart film technology at the time of this thesis’ submission limited experiments to experimental modal analysis of silicon wafers with tightly controlled boundary conditions. However, as the film growth capabilities mature to include growth on aluminum (for its stable surface chemistry) or iron samples, vibroacoustic characterization of these films presents itself as a clearly interesting next step. When the film reaches stability in an operating pipe, the questions of how flow affects chelation, how film cross-linking will reveal itself in operating vibroacoustic data, and the degree to which the film can localize mass transfer from the inner diameter of a pipe would all be of interest. A more tractable first step, however, might be to characterize the vibroacoustic properties of smart films saturated with water because the films become much more gelatinous when they are saturated with water. The sensitivity challenges experienced in this research may be mitigated by the increased mass of the water-film matrix and by taking non-contact measurements for frequency response function estimation.

References

- [1] European Commission, “Report on the regulatory experience of risk-informed inservice inspection of nuclear power plant components and common views,” no. August, pp. 1–90, 2004.
- [2] N. P. Reactors, “REFERENCE DATA SERIES No. 2 2018 Edition - Nuclear Power Reactors in the World,” no. 2, p. 79, 2018.
- [3] World Nuclear Association, “World Nuclear Performance Report,” *World Nucl. Assoc.*, vol. 1, p. 32, 2018.
- [4] World Nuclear Association, “US Operating Nuclear Reactors,” 2019. [Online]. Available: <http://www.world-nuclear.org/information-library/country-profiles/countries-t-z/appendices/nuclear-power-in-the-usa-appendix-1-us-operating-n.aspx>.
- [5] U. E. I. Agency, “U . S . Nuclear Industry – Basics,” pp. 1–3, 2019.
- [6] F. Cattant, D. Crusset, and D. Féron, “Corrosion issues in nuclear industry today,” *Mater. Today*, vol. 11, no. 10, pp. 32–37, 2008.
- [7] C. Group, “Operating Experience Insights into Pressure Boundary Component Reliability and Integrity Management Topical Report by the Component,” 2017.
- [8] S. H. Bush and A. D. Chockie, “SKI Report 96 : 20 Piping Failures in United States Nuclear Power Plants : 1961-1995 SKI Report 96 : 20 Piping Failures in United States Nuclear Power Plants .;,” no. January, pp. 1961–1995, 1996.
- [9] M. Kutz, *Handbook of Environmental Degradation of Materials*. 2018.
- [10] O. Nuclear and E. Agency, “NEA / CNRA / R (2014) 1 Unclassified ORGANISATION FOR ECONOMIC CO-OPERATION AND DEVELOPMENT,” pp. 1–40, 2014.
- [11] B. D. Williams, I. D. Editor, and P. N. C. Hyatt, “Offline reactor costing EDF \$1.2m per day 02/22/2017,” pp. 1–2, 2019.
- [12] P. Bacqué and R. T. Sep, “Nuclear plant outages costly,” pp. 1–6, 2019.
- [13] A. Exhibit and O. Wyman, “Financial Planning to Improve Nuclear Refueling Outages Performance,” 2001.
- [14] U. S. E. I. Administration, “Levelized Cost and Levelized Avoided Cost of New Generation Resources in the Annual Energy Outlook 2018,” 2018.
- [15] W. A. Soares, V. De Vasconcelos, and E. G. Rabello, “Risk-Based Inspection in the Context of Nuclear Power Plants,” *Int. J. Nucl. Atl. Conf. - Ina. 2015*, 2015.
- [16] President’s Commission on The Accident at Three Mile Island, “The Need for Change: The legacy of Three Mile Island,” 1979.
- [17] INSAG, *The Chernobyl Accident: Updating of INSAG-1 (Safet Series 75-INSAG-7)*, no. 75. 1992.
- [18] V. K. Chexal and R. L. Jones, “Implications of the surry piping failure for other nuclear and fossil units,” *Int. J. Press. Vessel. Pip.*, vol. 34, no. 1–5, pp. 331–343, 1988.
- [19] IAEA, *The International Chernobyl Project Technical Report: assessment of radiological consequences and evaluation of protective measures. Report by an International Advisory Committee.*, vol. 21, no. 1. 1994.
- [20] IAEA Nuclear Energy Series, “Risk-informed in-service inspection of piping systems of nuclear power plants: process, status, issues and development,” pp. 1–42, 2010.
- [21] ASME, “Pressure Vessel Code Section XI: Rules for In-service Inspection of Nuclear Power Plant Components.” ASME, 2001.

- [22] G. Koppen, “Development of Risk-Based Inspection,” in *Proceedings of the First International Conference on NDE Relationship to Structural Integrity for Nuclear and Pressurised Components*, 1998, pp. 20–22.
- [23] J. Gaertner, K. Canavan, and D. True, “Safety and Operational Benefits of Risk-Informed Initiatives,” no. February, p. 3, 2008.
- [24] D. J. Naus, “Inspection of Nuclear Power Plant Structures – Overview of Methods and Related Applications,” 2009.
- [25] J. D. Wood, “Methods of Nondestructive Evaluation,” 1989.
- [26] T. J. Johnson and D. E. Adams, “Transmissibility as a Differential Indicator of Structural Damage,” *J. Vib. Acoust.*, vol. 124, no. 4, p. 634, 2002.
- [27] T. J. Johnson, R. L. Brown, D. E. Adams, and M. Schiefer, “Distributed structural health monitoring with a smart sensor array,” *Mech. Syst. Signal Process.*, vol. 18, no. 3, pp. 555–572, 2004.
- [28] T. Takano, T. Yamagata, Y. Sato, and N. Fujisawa, “Non-Axisymmetric Mass Transfer Phenomenon behind an Orifice in a Curved Swirling Flow,” *J. Flow Control. Meas. & Vis.*, vol. 01, no. 01, pp. 1–5, 2013.
- [29] M. Matsumura, “A case study of a pipe line burst in the Mihama nuclear power plant,” *Mater. Corros.*, vol. 57, no. 11, pp. 872–882, 2006.
- [30] X. Deng, “Surface-initiated ring opening metathesis polymerization from the vapor phase to prepare compositionally versatile thin films,” Vanderbilt University, 2018.
- [31] M. Analysis, M. Stiffness, and D. Matrix, “MITOCW | 24. Modal Analysis: Orthogonality, Mass Stiffness, Damping Matrix,” pp. 1–25.
- [32] R. R. Craig and A. J. Kurdila, *Fundamentals of Structural Dynamics*, 2nd ed. 2006.
- [33] F. Magalhães and Á. Cunha, “Explaining operational modal analysis with data from an arch bridge,” *Mech. Syst. Signal Process.*, vol. 25, no. 5, pp. 1431–1450, 2011.
- [34] B. Peeters and G. De Roeck, “Reference-Based Stochastic Subspace Identification for Output-Only Modal Analysis,” *Mech. Syst. Signal Process.*, vol. 13, pp. 855–878, 1999.
- [35] Á. Cunha, E. Caetano, and F. Magalhães, “Output-only dynamic testing of bridges and special structures,” *Struct. Concr.*, vol. 8, no. 2, pp. 67–85, 2007.
- [36] C. Kramer, C. A. M. DeSmet, and B. Peeters, “Comparison Of Ambient And Forced Vibration Testing Of Civil Engineering Structures,” *Proc. IMAC 17, Int. Modal Anal. Conf.*, vol. 1, pp. 1030–1034, 1999.
- [37] R. J. Shaefer, “Mechanical Properties of Rubber.” pp. 381–410, 2016.
- [38] S. J. Li, G. M. Liu, and W. T. Kong, “Vibration analysis of pipes conveying fluid by transfer matrix method,” *Nucl. Eng. Des.*, vol. 266, pp. 78–88, 2014.
- [39] A. S. Tijsseling, “Fluid-structure interaction in liquid-filled pipe systems: sources, solutions and unsolved problems,” *TU Eindhoven*, vol. 0205, no. 2002, 2002.
- [40] J. Gale, I. T. Jo, and I. Tiselj, “Eight Equation Model for Arbitrary Shaped Pipe Conveying Fluid,” *Int. Conf. Nucl. Energy New Eur.*, no. September, pp. 1–10, 2006.
- [41] S.-S. Chen, “ARGONNE NATIONAL LABORATORY, ARGONNE, ILLINOIS Operated by THE UNIVERSITY OF CHICAGO for the U. S. DEPARTMENT OF ENERGY under Contract W-31-109-Eng-38.”
- [42] M. K. Au-Yang, *Flow-induced vibration of power and process plant components: a practical workbook*. ASME Press, 2001.
- [43] M. Hopcroft, “What is the Young ’ s Modulus of Silicon? What is the Crystal Orientation in a Silicon

Wafer ?," *Phys. Acoust.*, vol. 19, no. 2, pp. 229–238, 2007.

- [44] N. Gajendar, "Free Vibrations of a Circular Plate with Attached Concentrated Mass, Spring, and Dashpot," *J. Soc. Ind. Appl. Math.*, vol. 10, no. 4, pp. 668–674, 1966.